Indirect Optimization of Planetocentric Solar Sail Trajectories for Circular Orbit Transfers

Oskar Miller

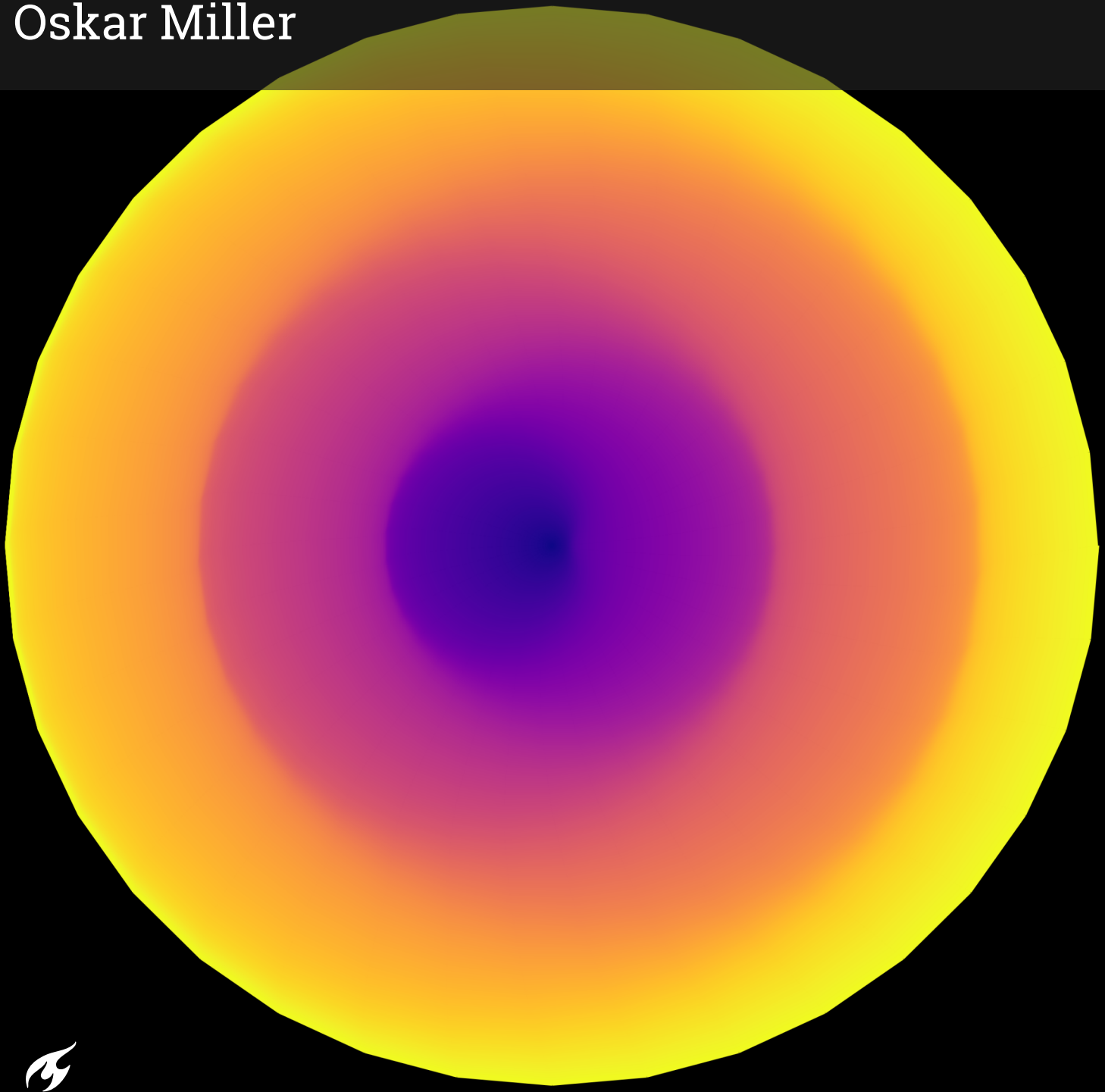

Delft University of Technology

TU Delft

Indirect Optimization of Planetocentric Solar Sail Trajectories for Circular Orbit Transfers

by

Oskar Miller

Student Name	Student Number
Oskar Miller	5283507

Supervisor:	Dr. Ir. J. Heiligers
Co-Supervisor:	Ir. F. Gámez Losada
Project Duration:	February, 2025 - November, 2025
Faculty:	Faculty of Aerospace Engineering, Delft

Cover: 1000-revolution transfer, 4 eccentricity reversals visible. Author's own work.

TU Delft

Preface

This work marks, hopefully, the conclusion of my academic journey at TU Delft. I would like to thank my family and my girlfriend for standing by me throughout these five years. The time has passed faster than I ever expected, and along the way, I've made some lifelong friends.

Regarding the work itself, I would first like to thank my daily supervisor, Fernando. Although we've only been in the same room a handful of times, your guidance has been instrumental in bringing this work to life. I also want to thank Jeannette Heiligers for allowing me to join the research group and for her help both technically and in reporting. Finally, I'm grateful to the solar sailing research group at Delft, especially Varun and Federico. Sharing this thesis journey with all of you has been a pleasure, and learning from such talented people has been invaluable. Thank you!

Oskar Miller
Delft, November 2025

Summary

Solar sailing is a propellantless propulsion method that uses a thin reflective membrane to convert the momentum of photons from sunlight into acceleration. The advantage of solar sailing over traditional means of propulsion is the absence of propellant, which makes solar sailing an attractive option for long-duration missions such as station-keeping and repeated debris removal. As the technology is fairly recent, there is little literature on how to optimally solar sail, and most of the research is conducted for heliocentric solar sailing. However, most of the technical demonstrations of solar sailing have been Earth-bound, which shows that there is also a need to know how to sail in planetocentric configurations.

Planet-centered sailing is considerably more complex than Sun-centered sailing for several reasons. The gravitational acceleration of the central body is orders of magnitude larger than the acceleration produced by the solar sail, which limits the sail's control authority and leads to long-duration, many-revolution transfers. In addition, the orientation of the Sun line relative to the sail and the orbital plane continuously changes due to the local orbiting of the sail around the central body and the central body's orbit around the Sun, resulting in highly complex control profiles. A fundamental building block of these long-duration solar-sail transfers is the circular-to-circular (C2C) transfer, which has so far only been studied using direct optimal control methods and differential dynamic programming (DDP). This study aims to solve and characterize the planar planetocentric C2C solar-sail transfer optimal control problem (OCP) using indirect optimal control methods, which have thus far been avoided due to their sensitivity to initial guesses.

The dynamics are formulated in a polar coordinate system using an ideal sail model and scaling for better numerical stability. The indirect OCP is set up using the Calculus of Variations and Pontryagin's Maximum Principle (PMP). A key step in formulating the problem is using PMP to write the control input as a function of the costates for which the dynamics are known based on the objective and the Hamiltonian. This formulation allows the otherwise infinite-dimensional problem to be set up as a finite-dimensional two-point boundary value problem (TPBVP). Compared to direct optimal control and DDP, where the full control profile is needed as an initial guess, the indirect problem formulation only needs the guess of the costate and Lagrange multiplier values at the initial time. The problem is then solved using a single-shooting method.

This solver framework is then applied to many-revolution planetocentric transfers with the aim of characterizing the optimal sail behavior and the transfer performance. In this context, the transfer performance is quantified by the radius gain in a given transfer duration. The analysis also examines phasing effects, which describe the relative geometry between the Sun direction and the orbital plane at the start of the transfer. Laws are identified that produce both favorable and unfavorable phasing conditions. Based on the phasing and transfer duration, the transfer performance envelopes are defined, which give an overview of the possible range of transfer performances given a sail design, orbital geometry, and transfer duration.

The convergence, sensitivity, and robustness of the framework are analyzed to quantify the weakness of the indirect method, which is its sensitivity to initial guesses. It is found that solution elements vary smoothly with the orbital parameters, sail design, and transfer duration, which indicates that continuation methods could work to reach convergence for difficult transfer configurations that would otherwise not converge from a trivial initial guess. Furthermore, convergence basins were analyzed for a range of transfer parameters, revealing a number of noteworthy trends that could improve the manner in which initial guesses are generated.

The developed algorithm exceeded expectations in convergence and computational speed when applied to many-revolution C2C transfers. Additionally, the solutions were validated against state-of-the-art direct solvers. The developed framework is a good baseline to expand the analysis by including non-ideal sail models and adding perturbing forces. The characteristics found in this study for the ideal

C2C planetocentric solar-sail transfers could be extrapolated to higher-fidelity models to validate and expand them.

Contents

List of Figures

List of Tables

Nomenclature

Abbreviations

Abbreviation	Definition
AA	Aspect Angle (angle between Sun-line and orbital angular momentum vector)
ACS3	Advanced Composite Solar Sail System
AU	Astronomical Unit
C2C	Circular-to-Circular
CoV	Calculus of Variations
DDP	Differential Dynamic Programming
EoM	Equations of Motion
GEO	Geostationary (or geosynchronous) Equatorial Orbit
GPOPS-II	Gauss/General Pseudospectral Optimal Control Software II (direct collocation solver)
GTO	Geostationary Transfer Orbit
ICRF	International Celestial Reference Frame
IKAROS	Interplanetary Kite-craft Accelerated by Radiation Of the Sun
IQR	Interquartile Range
LEO	Low Earth Orbit
MEO	Medium Earth Orbit
NASA	National Aeronautics and Space Administration
NLP	Nonlinear Program
OCP	Optimal Control Problem
ODE	Ordinary Differential Equation
PCI	Primary-Centered Inertial reference frame
PID	Proportional–Integral–Derivative controller
PMP	Pontryagin's Maximum Principle
RAAN	Right Ascension of the Ascending Node
RTN	Radial–Tangential–Normal reference frame
SLF	Sunlight Fixed
SRP	Solar Radiation Pressure
SSA	Solar-Sail Acceleration
TPBVP	Two-Point Boundary Value Problem

Symbols

Symbol	Definition	Unit
A	Sail surface area	[m^2]
a_0	Characteristic acceleration of the sail at the primary's heliocentric distance	[mm/s^2]
a_R	Radial component of solar-sail acceleration (RTN frame)	[m/s^2]
a_T	Tangential component of solar-sail acceleration (RTN frame)	[m/s^2]
a_N	Normal component of solar-sail acceleration (RTN frame)	[m/s^2]
$\boldsymbol{a}_{SLF}$	Solar-sail acceleration vector in the SLF frame	[m/s^2]
$\boldsymbol{a}_S$	Solar-sail acceleration vector in SLF frame	[m/s^2]

Symbol	Definition	Unit
$\boldsymbol{a}_O$	Solar-sail acceleration vector in RTN frame	[m/s^2]
c	Speed of light	[m/s]
Δr	Change in orbital radius over the transfer, $\Delta r = r_f - r_0$	[m] or [km]
e	Scalar eccentricity (magnitude of $\boldsymbol{e}$)	[-]
$\boldsymbol{e}$	Eccentricity vector (in PCI frame, apoapsis–periapsis direction)	[-]
H	Hamiltonian	[-]
$\mathcal{H}$	Part of the Hamiltonian that is dependent on control	[-]
i	Inclination of the orbit	[rad] or [°]
J	Performance index (cost functional)	[-]
J_2	Second zonal harmonic coefficient of the primary's gravity field	[-]
L	Lagrangian (running cost)	[-]
$\mathcal{L}_S$	Solar luminosity	[W]
L_s	Solar longitude along the primary's orbit	[rad] or [°]
m	Total spacecraft mass	[kg]
n	Dimension of the state vector	[-]
p_a	Power-law exponent of transfer performance w.r.t. Π_a	[-]
p_r	Power-law exponent of transfer performance w.r.t. Π_r	[-]
P	Solar radiation pressure	[N/m^2]
P_E	Solar radiation pressure at 1 AU (Earth distance)	[N/m^2]
$\mathcal{P}$	Transfer performance; radius change over initial radius, $\mathcal{P} = r_f/r_0 - 1$	[-]
q	Number of terminal constraints	[-]
R_E	Sun–Earth distance	[m]
r	Radial distance from the primary	[m]
r_0	Initial orbital radius	[km] or [m]
r_f	Final orbital radius	[km] or [m]
r_s	Sun–spacecraft distance	[m]
S	Sun-line drift over the transfer, $S \equiv \omega t_f$	[rad]
$\dot{S}$	Sun-line drift per orbit, $\dot{S} \equiv 2\pi\omega\sqrt{r_0^3/\mu}$	[rad/orbit]
t	Time	[s]
t_0	Initial time (epoch)	[s]
t_f	Final time / time of flight (transfer duration)	[s] or [yr]
u	Radial velocity	[m/s]
U	Admissible control set	[-]
v	Tangential velocity	[m/s]
v_0	Initial circular velocity (for scaling)	[m/s]
W	Radiative energy flux (irradiance)	[W/m^2]
$\mathcal{W}$	Jacobian matrix of $\boldsymbol{F}(\boldsymbol{w})$ w.r.t. $\boldsymbol{w}$	[-]
W_E	Solar constant at 1 AU	[W/m^2]
$\mathcal{I}_P$	Primary-Centered Inertial frame (PCI)	[-]
$\mathcal{S}$	Sunlight Fixed frame (SLF)	[-]
$\mathcal{O}$	Radial–Tangential–Normal frame (RTN)	[-]
$\hat{X}, \hat{Y}, \hat{Z}$	Unit vectors of PCI frame	[-]
$\hat{x}, \hat{y}, \hat{z}$	Unit vectors of SLF frame	[-]
$\hat{R}, \hat{T}, \hat{N}$	Unit vectors of RTN frame	[-]
$\hat{s}$	Sun-line unit vector (Sun to spacecraft)	[-]
$\hat{h}$	Orbital angular momentum unit vector	[-]
$\bar{t}$	Scaled time, $\bar{t} = t/t_f$	[-]
$\bar{r}$	Scaled radius, $\bar{r} = r/r_0$	[-]
$\bar{u}$	Scaled radial velocity, $\bar{u} = u/v_0$	[-]
$\bar{v}$	Scaled tangential velocity, $\bar{v} = v/v_0$	[-]
$\boldsymbol{x}$	State vector (e.g. $\boldsymbol{x} = [r, \theta, u, v]^T$ or $[r, t, u, v]^T$)	[-]

Symbol	Definition	Unit
$\boldsymbol{x}_0$	Initial state vector	[-]
$\boldsymbol{u}$	Control-input vector (sail orientation)	[-]
$\boldsymbol{f}$	State dynamics function	[-]
$\boldsymbol{q}$	Primer vector (optimal thrust direction)	[-]
$\boldsymbol{w}$	Combined unknown vector (initial costates and Lagrange multipliers)	[-]
$\boldsymbol{w}^\star$	Benchmark (reference) solution vector	[-]
$\boldsymbol{F}(\boldsymbol{w})$	TPBVP shooting function	[-]
l	Perturbation magnitude applied to the solution vector	[-]
α	Cone angle between Sun-line and sail normal	[rad]
δ	Clock angle (azimuth of sail normal about Sun-line)	[rad]
δ_0	Start-phase of the transfer, $\delta_0 \equiv \Omega - L_s(t_0)$	[rad] or [°]
ϕ	Auxiliary angle between primer vector and Sun-line in sail steering law	[rad]
$\phi(t_f, \boldsymbol{x}_f)$	Terminal cost (part of the performance index)	[-]
θ	Argument of latitude (in-plane angular position)	[rad]
θ_f	Final accumulated argument of latitude	[rad] or [rev]
$\bar{\theta}$	Scaled argument of latitude, $\bar{\theta} = \theta/\theta_f$	[-]
κ	Condition number $\kappa = \sigma_{\max}/\sigma_{\min}$	[-]
$\boldsymbol{\lambda}$	Costate (adjoint) vector	[-]
$\lambda_{\bar{r}}$	Costate associated with $\bar{r}$	[-]
$\lambda_{\bar{t}}$	Costate associated with $\bar{t}$	[-]
$\lambda_{\bar{u}}$	Costate associated with $\bar{u}$	[-]
$\lambda_{\bar{v}}$	Costate associated with $\bar{v}$	[-]
$\boldsymbol{\Lambda}_0$	Vector of initial costates	[-]
μ	Gravitational parameter of the primary	[m^3/s^2]
ν_1, ν_2	Components of the terminal Lagrange multiplier vector	[-]
$\boldsymbol{\nu}$	Lagrange multiplier vector for terminal constraints	[-]
Σ	Transversality condition function	[-]
Ω	Right Ascension of the Ascending Node (RAAN)	[rad] or [°]
ω	Mean motion of the primary's orbit around the Sun	[rad/s]
Φ	Terminal function (augmented terminal cost)	[-]
$\boldsymbol{\Psi}$	Terminal constraint vector (e.g. circularity conditions)	[-]
Π_a	Dimensionless sail-strength group, $\Pi_a \equiv a_0/(\mu^{1/3}\omega^{4/3})$	[-]
Π_r	Dimensionless radius group, $\Pi_r \equiv r_0\omega^{2/3}/\mu^{1/3}$	[-]
Π_t	Dimensionless time (duration) group, $\Pi_t \equiv \omega t_f$	[-]
ρ_{ij}	Radius of the 2D vector formed by components $(w_i^\star, w_j^\star)$ in polar decomposition	[-]
β_{ij}	Angle of the 2D vector $(w_i^\star, w_j^\star)$ in polar decomposition	[rad]
$\sigma_{\max}$	Largest singular value	[-]
$\sigma_{\min}$	Smallest singular value	[-]
ξ	Scaled characteristic acceleration, $\xi \equiv a_0 r_0^2/\mu$	[-]
η	Perturbation direction (unit vector on six-dimensional unit sphere), components of $\boldsymbol{\eta}$	[-]

1

Introduction

Solar sailing is a propellant-free spacecraft propulsion method that utilizes the momentum carried by sunlight. Rather than burning fuel, solar sails employs a large, lightweight, highly reflective membrane to convert photon pressure into continuous thrust [1]. With origins tracing back to early astronomical observations and theoretical developments, solar sailing was largely a theoretical curiosity until engineering studies showed its feasibility during the second half of the 20th century [2]. Significant practical demonstration missions have occurred in the early 21st century, such as Japan's IKAROS mission [3] in 2010 and NASA's Advanced Composite Solar Sail System (ACS3) in early 2024 [4], which have cemented solar sailing as a realistic propulsion technology.

Along with the practical demonstrations has come an increased need for solar-sail trajectory optimization research. While the early body of literature was mainly aimed at heliocentric solar-sail trajectories [5]–[8], there has also been a growing interest in planetocentric applications ranging from orbit-raising to station-keeping [9], [10]. The limitations for planetocentric solar sailing are nontrivial. Due to the small acceleration magnitude that the sail provides, the control authority is limited, and the thrust is inherently constrained by the direction of sunlight. Additionally, there is the effect of eclipses, during which no thrust can be generated. Due to these limitations, solar-sail planetocentric transfers are often highly nonlinear and require long transfer times [1].

In this thesis, the planar planetocentric circular-to-circular solar-sail transfer optimal control problem is set up and solved using indirect methods. The characteristics of these transfers are then analyzed to derive a broader understanding of optimal solar-sail transfers around planetary bodies. The thesis is structured as follows. First, a literature study is presented in Chapter 2. Then, the main content and body of work are presented in a journal paper format in Chapter 3. Finally, the results are summarized in Chapter 4, together with recommendations for future work.

2

Literature Study

This chapter reviews the key literature on solar sailing and indirect optimal control, forming the foundation for the formulation of the research objectives. The fundamentals of solar sailing, along with a brief overview of its research history, are presented in Section 2.1, while Section 2.2 focuses on the operational aspects and studies of planetocentric solar sailing. The principles of indirect optimal control are discussed in Section 2.3, and finally, Section 2.4 presents the research objectives and corresponding research questions.

2.1. Fundamentals of Solar Sailing

Solar sailing is a method of spacecraft propulsion that requires no propellant, relying instead on the momentum transferred from sunlight. Rather than consuming fuel, it uses a large, lightweight, and highly reflective membrane to convert photon pressure into continuous thrust [1]. This section presents the fundamental physical principles of solar sailing in Section 2.1.1 and provides a brief history of solar sailing research and missions in Section 2.1.2.

2.1.1. Physical Principles

This subsection derives the force exerted by solar radiation on a solar sail and is primarily based on Ref. [1], unless stated otherwise. Several simplifying assumptions are made: the sail perfectly absorbs and reflects radiation, incident radiation can be treated as parallel beams of light, and the sail is infinitely rigid. The pressure exerted on a surface by photon momentum transfer is given as:

$$P = \frac{W}{c}, \tag{2.1}$$

where W is the energy flux (the energy crossing a unit area in unit time) and c is the speed of light ($c = 299792458\frac{m}{s}$). The energy flux at the distance between the Earth and the Sun, denoted W_E, is given by:

$$W_E = \frac{\mathcal{L}_S}{4\pi R_E^2}, \tag{2.2}$$

where $\mathcal{L}_S$ is the solar luminosity and R_E is the Sun–Earth distance. This equation can be generalized for any arbitrary distance from the Sun r_s:

$$W = W_E \left(\frac{R_E}{r_s}\right)^2. \tag{2.3}$$

Due to the elliptical orbit of the Earth around the Sun, the energy flux at Earth varies by approximately 3.5% annually. Nonetheless, a standard solar constant $W_E = 1361\frac{W}{m^2}$ is commonly accepted for Earth.

Substituting the solar constant into Equation (2.1), the SRP at 1 astronomical unit (AU) becomes $P_E = \frac{W_E}{c} = 4.54 \cdot 10^{-6} \frac{N}{m^2}$.

The solar-sail performance can then be characterized using the characteristic acceleration a_0 which represents the acceleration achievable at 1 AU for a flat and rigid, perfectly specularly reflecting, fully illuminated solar sail oriented perpendicular to incoming SRP. The characteristic acceleration is defined as:

$$a_0 \triangleq 2\frac{P_E A}{m}, \tag{2.4}$$

where m is the total spacecraft mass and A is the sail surface area.

Under the assumption of a specularly reflecting sail, the solar radiation pressure (SRP) produces an acceleration along the sail-normal vector $\hat{n}$, directed away from the Sun. The orientation of the sail-normal is defined in the Sun-Light Fixed (SLF) reference frame, where the $\hat{x}$-axis is aligned with the Sun-line and points away from the Sun, the $\hat{z}$-axis is parallel to the normal of the orbital plane of the sail, and the $\hat{y}$-axis completes the right-handed triad. The orientation of the sail-normal within the SLF frame is illustrated in Figure 2.1.

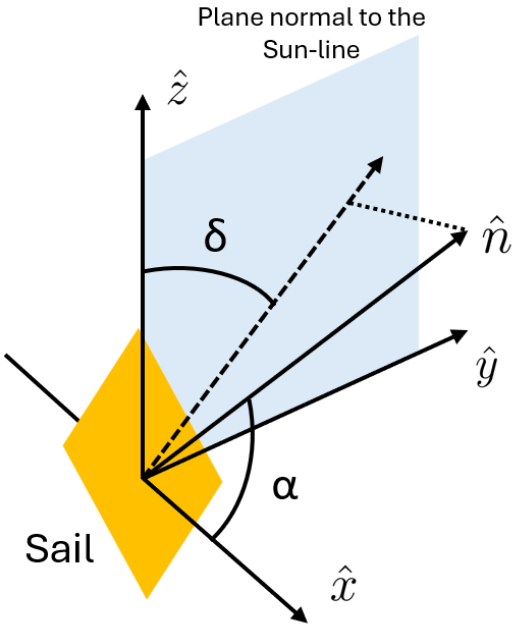

Figure 2.1: Illustration of the cone angle α and clock angle δ

Two angles define the orientation of the sail-normal: the *cone angle* α and the *clock angle* δ. As seen in Figure 2.1, the cone angle is the angle between the Sun-line $\hat{x}$ and the sail-normal vector $\hat{n}$, indicating the degree of sail illumination. The clock angle specifies the azimuthal orientation of the sail, defined as the angle between the projection of $\hat{n}$ onto the $\hat{y}\hat{z}$-plane and the positive $\hat{z}$-axis, increasing toward the positive $\hat{y}$-direction. The solar-sail acceleration vector can then be defined in the SLF frame as:

$$\boldsymbol{a}_{SLF} = a_0 \cos^2\alpha \left[\cos\alpha,\ \sin\alpha\sin\delta,\ \sin\alpha\cos\delta\right]^{\mathrm{T}}. \tag{2.5}$$

As the cone angle increases, the sail-normal vector rotates away from the Sun-line and the effective area of the sail decreases. The effect of the cone angle on the axial and transversal acceleration components is shown in Figure 2.2. As expected, the axial acceleration is the largest when the cone angle is $0°$ and the sail-normal is parallel to the Sun-line. The transversal acceleration however is the largest when the cone angle is approximately $35°$.

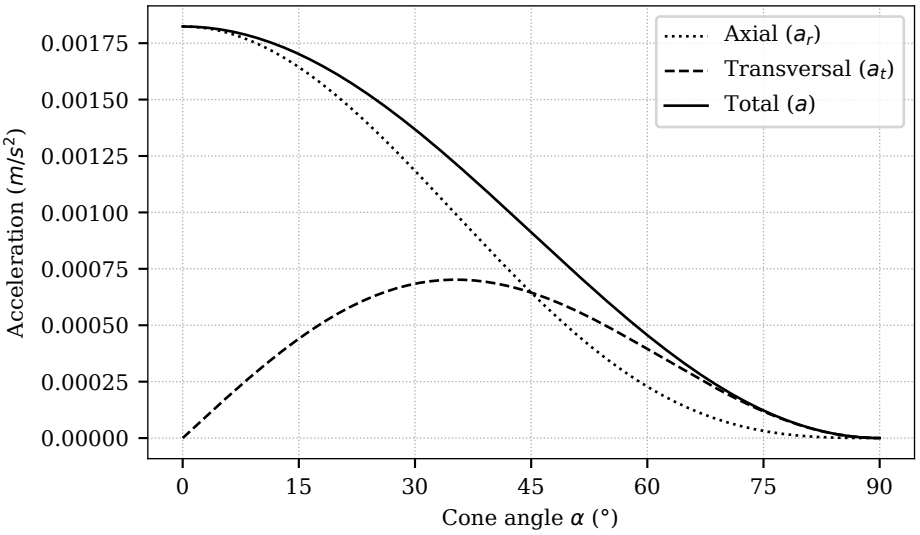

Figure 2.2: Solar-sail acceleration components as a function of cone angle α

2.1.2. Solar Sailing Research History

The first ideas of solar sailing date back to early astronomical observations when Johannes Kepler, observing comet tails in the 17th century, thought of a force exerted by sunlight. It was only in 1873, when James Clerk Maxwell demonstrated that electromagnetic radiation carries momentum and applies force on surfaces, that this thought became a real theory [1].

In the early 20th century, both Konstantin Tsiolkovsky and Friedrich Zander independently proposed the idea of using solar radiation for spacecraft propulsion. Engineering studies into the matter began shortly after that under the lead of Louis Friedman, Carl Sagan, and Jerome Wright. These early engineering studies transformed solar sailing from a theory to a realistic propulsion technology [2].

The first practical demonstrations started in the 21st century, with the IKAROS mission in 2010 being the first successful interplanetary solar sail. This validated the critical components of solar sailing, such as sail deployment, reflectivity modulation for attitude control, and measurable SRP acceleration [3]. Later, in 2019, the LightSail 2 mission from Planetary Society demonstrated controlled solar sailing in Earth orbit, raising orbital altitude using only SRP [11]. With the successful launch and deployment of the Advanced Composite Solar Sail System (ACS3) by NASA in early 2024, solar sailing is becoming a fully accepted form of low-thrust propulsion [4].

A need for trajectory optimization techniques has increased together with the development of solar-sailing technology. In the middle of the 20th century, the first analytical studies were done which explored the theoretical limits of solar-sail propulsion [12], [13]. By the 1970s, optimization techniques, including calculus of variations (CoV), were applied by researchers which laid the base for modern trajectory optimization methods.

At the end of the 20th century and the beginning of the 21st, there was an accelerated development of trajectory optimization methods due to computational advancements in the same period. However, while heliocentric trajectory optimization has the largest body of literature [5]–[8], practical missions have mostly been planetocentric demonstrations. Consequently, addressing the current research gap requires further investigation into planetocentric solar sail dynamics and trajectory optimization techniques.

2.2. Planetocentric Solar Sailing

This section gives an overview of the optimization of solar-sail trajectories in planetocentric environments. Section 2.2.1 begins by detailing the operational aspects that affect planetocentric transfers, such as changing illumination, periodic eclipses, and various perturbing forces that do not exist in he-

liocentric dynamics. The existing body of research on planetocentric solar-sail trajectory optimization is then reviewed in Section 2.2.2 to identify current limitations and gaps in the literature.

2.2.1. Operational Aspects

Solar sailing around a planet introduces several operational complexities that would not be present when performing heliocentric transfers. These operational aspects are explained below.

Varying Illumination Geometry

In heliocentric missions, the relative geometry between the Sun and the spacecraft remains nearly constant over time, allowing the sail to maintain a fixed or slowly varying orientation with respect to the sunlight which results in smooth and predictable attitude-control profiles [1]. In contrast, for planet-centered sailing, the illumination conditions are generally time-varying. Because the spacecraft orbits the planet while the planet itself moves around the Sun, the direction of the Sun-line continuously changes with respect to both the local orbital frame and the spacecraft's velocity vector [1], [14]. This relative motion of the Sun-line influences the achievable thrust direction and magnitude, often complicating the generation of efficient control profiles. The most efficient thrust is typically achieved when the sail acceleration is aligned with the velocity vector; however, during orbital segments when the spacecraft moves toward the Sun, the sail cannot generate positive thrust in the direction of motion. As a result, the optimal sail orientation tends to vary throughout the orbit, except in specific configurations where the orbital plane is nearly perpendicular to the Sun-line and illumination conditions remain relatively constant [1], [15].

Eclipses and Occultation

Depending on the orbital geometry and altitude, planetocentric orbits could involve periodic eclipses during which the spacecraft enters the shadow of the planet it is orbiting and temporarily loses the ability to generate thurst. These eclipse periods interrupt continuous thrust generation and must be taken into account during mission design. Recent studies have highlighted significant impacts of eclipse constraints on optimized planetocentric solar-sail trajectories [16], [17].

Perturbing Forces

In addition to solar radiation pressure and gravitational attraction by the central planet, planetocentric orbits experience various perturbing forces. These include aerodynamic drag, non-spherical gravity, and planetary radiation pressure. Numerous studies have demonstrated the importance of these perturbations on spacecraft dynamics and trajectories [17]–[20]. Additionally, Earth-orbiting solar sails may face increased collision risks from orbital debris due to their large size, necessitating collision avoidance maneuvers and imposing further operational constraints [21], [22].

Dynamical Considerations

Due to these operational complexities and the inherently constrained magnitude and direction of solar-sail acceleration, planetocentric orbit transfers typically involve extended durations and complex multi-revolution trajectory optimization problems, which are inherently more challenging to optimize than single-revolution transfers [23].

2.2.2. Previous Work on Planetocentric Solar Sailing Trajectory Optimization

Planetocentric solar-sail transfers were first comprehensively studied by Sackett in 1977, who analyzed optimal open-ended spiral trajectories using indirect optimization methods for transfers such as Earth orbit raising and escape trajectories [24]. The paper, together with the introduction of the SUNSPOT software the same year [25], was the basis for studies into optimal planet-centered solar sailing.

In 2003, Coverstone and Prussing introduced elementwise locally optimal control laws, focusing on controlling specific orbital elements. Their work examined gravitational escape trajectories from geostationary transfer orbits (GTOs) [26]. A few years later, in 2005, Mengali and Quarta analyzed time-optimal orbit-raising maneuvers from low Earth orbits using similar methods [18]. In the same year, Macdonald and McInnes expanded these locally optimal control laws by using blended locally optimal control, which combines multiple elementwise optimal strategies. These methods were successfully applied to Earth-escape trajectories and orbit station-keeping tasks [9], [10]. Further applications of

these locally optimal and blended strategies include optimal orbital parameter changes [14], [20], [27] and specific mission scenarios [28].

Locally optimal control laws are simple and computationally efficient, which explains their extensive use. Recent advancements in computational power and algorithms, however, have increased interest in optimal control theory approaches, including indirect and direct methods. For example, in 2019, Kelly et al. used Lyapunov-based indirect methods to optimize geostationary-to-graveyard orbit transfers [29]. Hybrid methods incorporating eclipse constraints were later employed by the same authors [16]. Additionally, optimal steering laws for unbounded orbit raising were derived using indirect methods by Barles et al. in 2021 [30], while Leemans et al. applied differential dynamic programming (DDP) to analyze optimal transfers focused on orbital energy increase [31].

Although extensive research has focused on heliocentric and open-ended Earth-escape trajectories using locally optimal or hybrid methods, fewer studies have investigated planetocentric orbit-to-orbit transfers or rendezvous trajectories. Most existing studies addressing specific orbit transfers primarily focus on mission-specific applications [16], [24], [32]. Thus, general characterization of orbit-to-orbit transfers remains limited. In 2024, Losada et al. presented a preliminary analysis of one-revolution planar planetocentric orbit transfers using direct optimization methods [33], and Minnozzi et al. demonstrated the ability of DDP to solve many-revolution Earth-centered planar C2C transfers [34]. The C2C transfer represents a fundamental building block for more complex long-duration trajectories as it forms the basis of multi-revolution orbit raising, phasing, and rendezvous maneuvers. Nevertheless, a comprehensive theoretical characterization of C2C planetocentric solar-sail transfers using indirect optimal control methods remains unexplored.

2.3. Indirect Optimization

Optimal control problems (OCPs) are commonly solved using either direct or indirect methods [35]. Direct methods transform the continuous OCP into a parameterized optimization problem by discretizing the system dynamics and then applying nonlinear programming techniques [36]. Direct methods are generally robust to initial guesses, but they require discretization and nonlinear programming, which means that computational cost increases drastically with problem size. In contrast, indirect methods derive the necessary conditions for optimality using CoV and Pontryagin's Maximum Principle (PMP). The problem is reduced to a finite-dimensional two-point boundary value problem (TPBVP) and solved using shooting methods. Due to the use of CoV and PMP, the resulting solutions are truly optimal and continuous, but that comes at the cost of the problem being highly sensitive to the initial guess leading to poor convergence. This section is dedicated to the formulation and numerical solution of OCPs using indirect methods. Section 2.3.1 presents the mathematical formulation of the problem, while Section 2.3.2 reviews the numerical techniques used to solve the resulting TPBVP.

2.3.1. Problem Formulation

This subsection is primarily based on Ref. [37], unless stated otherwise. The general formulation of an OCP is given by:

Minimize:

$$J = \phi(t_f, \boldsymbol{x}_f) + \int_{t_0}^{t_f} L(t, \boldsymbol{x}, \boldsymbol{u})\, dt, \tag{2.6}$$

where J is the performance index to be minimized, ϕ is the terminal cost, t_0 and t_f denote the initial and final times, $\boldsymbol{x}_f$ is the state at t_f, L is the Lagrangian, and $\boldsymbol{u}$ represents the control variables. This formulation is subject to the following constraints:

$$\dot{\boldsymbol{x}} = \boldsymbol{f}(t, \boldsymbol{x}, \boldsymbol{u}), \tag{2.7}$$

$$\boldsymbol{x}(t_0) = \boldsymbol{x}_0, \tag{2.8}$$

$$\boldsymbol{u} \in U, \tag{2.9}$$

$$\boldsymbol{\Psi}(t_f, \boldsymbol{x}_f) = \mathbf{0}. \tag{2.10}$$

Here, $\boldsymbol{f}(t, \boldsymbol{x}, \boldsymbol{u})$ defines the system dynamics, $\boldsymbol{\Psi}$ represents the terminal boundary conditions, and U is the set of admissible controls. The complete formulation in Equation (2.6) is known as the *Problem*

of Bolza. Removing the terminal cost yields the *Problem of Lagrange*, while removing the integral term produces the *Problem of Mayer*.

Equations (2.7), (2.8), and (2.10) define the state dynamics, initial conditions, and terminal constraints, respectively, while (2.9) restricts the control vector to U. The solution is obtained via the CoV, leading to the Euler-Lagrange equations. The Hamiltonian is defined as:

$$H(\boldsymbol{x}, \boldsymbol{\lambda}, \boldsymbol{u}, t) = L(\boldsymbol{x}, \boldsymbol{u}, t) + \boldsymbol{\lambda}^T \boldsymbol{f}(\boldsymbol{x}, \boldsymbol{u}, t), \tag{2.11}$$

and the terminal function is given by:

$$\boldsymbol{\Phi}(t_f, \boldsymbol{x}_f) = \phi(t_f, \boldsymbol{x}_f) + \boldsymbol{\nu}^T \boldsymbol{\Psi}(t_f, \boldsymbol{x}_f), \tag{2.12}$$

where $\boldsymbol{\lambda}$ is the vector of costate multipliers associated with the dynamics and $\boldsymbol{\nu}$ is a constant vector of multipliers for the terminal conditions.

The Euler-Lagrange equations provide the necessary conditions for optimality:

$$\dot{\boldsymbol{\lambda}}^T = -\frac{\partial H}{\partial \boldsymbol{x}} = -H_x, \tag{2.13}$$

$$\dot{\boldsymbol{x}} = H_\lambda, \tag{2.14}$$

$$H_u = \mathbf{0}. \tag{2.15}$$

Here, the subscript denotes partial differentiation with respect to the indicated variable. Equation (2.13) describes the dynamics of the costate variables, equation (2.14) reiterates the state dynamics (equation (2.7)), and equation (2.15) provides the control laws for $\boldsymbol{u}(t)$. When a definitive control cannot be obtained from equation (2.15), the PMP can be used, which states that the optimal control minimizes the Hamiltonian at each point along the trajectory. The principle is formalized in equation (2.16).

$$\frac{\partial^2 H}{\partial \boldsymbol{u}^2} \geq 0 \tag{2.16}$$

The resulting control can be substituted back into the state dynamics. The terminal boundary conditions of the costates are given by:

$$\boldsymbol{\lambda}(t_f) = \left(\frac{\partial \Phi}{\partial \boldsymbol{x}} \right)_{t=t_f} \tag{2.17}$$

When the final time is specified (e.g. single-revolution transfers where duration can be approximated as one orbital period), the stationary conditions from equation (2.15) determine the m-vector $\mathbf{u}(t)$, the $2n$ differential equations from equation (2.7) and equation (2.13) with $2n$ boundary conditions from equation (2.8) and equation (2.17), determine a TPBVP with constant q-vector $\boldsymbol{\nu}$ found in equation (2.17) so that the q terminal boundary conditions in equation (2.10) are satisfied [38].

However, when the final time is unspecified (e.g. for minimum time problems), the transversality condition needs to be defined:

$$\Sigma(t_f, \boldsymbol{x}_f, \boldsymbol{u}_f) = \left(L + \frac{d\Phi}{dt} \right)_{t=t_f} = \left(L + \frac{\partial \Phi}{\partial t} + \frac{\partial \Phi}{\partial \boldsymbol{x}} \boldsymbol{f} \right)_{t=t_f} = 0 \tag{2.18}$$

The vector $\mathbf{u}(t)$ is still given by equation (2.15) but this time t_f is added as an additional constant to determine in addition to the constant vector ν. Thus, the solution to the $2n$ differential equations in

equation (2.7) and equation (2.13) and the choice of the $q+1$ parameters ν and t_f are determined by the $2n+1+q$ boundary conditions from equation (2.8), equation (2.17), equation (2.18), and equation (2.10) [38].

2.3.2. Solution Methods

Due to the non-linearities in real-world systems, analytical solutions to the TPBVP are often impractical or impossible, making numerical techniques such as shooting methods a common approach.

The shooting method converts the TPBVP into an initial value problem by guessing the initial values for the costate variables, integrating the state and costate equations forward in time, and iteratively adjusting the initial guess until the terminal boundary conditions (Equation (2.10)) are satisfied within a prescribed tolerance. The error between the computed terminal state and the desired boundary conditions is reduced using iterative methods such as the Newton-Raphson technique. The multiple shooting method enhances numerical stability and robustness by dividing the integration interval into smaller subintervals, applying the shooting method on each segment, and ensuring continuity across the subintervals. This approach is particularly beneficial for highly non-linear systems [39].

A major drawback of shooting methods is their sensitivity to the initial guess for the costate variables. This issue has been addressed in several studies. For example, [40] employed adjoint-control transformations to generate more accurate initial guesses. [41] approximated the initial adjoint variables by solving equations in the neighborhood of the initial time using a first-order Taylor series expansion. More recent work has utilized analytical and shape-based approximations to estimate the initial costates for both general low-thrust transfers and heliocentric solar-sailing trajectories [42]–[45].

Further refinements to the shooting method have been developed to improve convergence and robustness. [46] introduced a method that constrains the shooting variables within a narrower solution space by incorporating physical insights, leading to faster and more robust convergence in time-optimal soft-landing problems. [47] proposed an indirect forward-backward shooting scheme that reduces solution sensitivity and can converge from a random initial guess in multibody dynamics. Finally, [48] presented a framework integrating PMP into the DDP formulation, which partially mitigates the sensitivity issues of indirect methods and enhances robustness.

2.4. Research Objective and Research Questions

Based on the research gaps identified in the previous sections, the research objective and research questions are stated in Section 2.4.1 and Section 2.4.2, respectively.

2.4.1. Research Objective

Planetocentric solar-sail transfers have so far been investigated primarily through locally optimal methods or numerical optimal-control techniques applied to specific mission scenarios or open-ended trajectories. Studies addressing fundamental transfer dynamics have mainly relied on direct methods or DDP. However, these approaches often provide limited analytical insight, since they treat the problem numerically and require heavy computation for each new set of boundary conditions. In contrast, an indirect optimal control formulation based on the CoV enables the derivation of necessary conditions for optimality in closed form, allowing a deeper understanding of the underlying dynamics and control structure. Such analytical characterization facilitates faster trajectory generation, parameter studies, and the validation of numerical methods. Therefore, this research aims to address the existing gap by developing and analyzing indirect CoV-based formulations for planetocentric solar-sail C2C transfers using shooting methods. Considering the sensitivity of the shooting methods to the initial guess, continuation methods will be employed and a detailed analysis will be performed to quantify the characteristics of the shooting methods for this specific set up. The research objective is defined as follows:

The research objective is to characterize planetocentric planar circular-to-circular transfers using solar sails by formulating the optimal control problem using calculus of variations and the Pontryagin's maximum principle and solving the resulting two-point boundary value problem (TPBVP) using shooting methods.

2.4.2. Research Questions

The presented research objective leads to the following research questions and sub-questions:

1. How can the planar circular-to-circular (C2C) solar-sail transfer around a planetary body be posed as a TPBVP using calculus of variations and Pontryagin's Maximum Principle?
2. How does the defined optimization algorithm perform, when applied to the identification of optimal planar circular-to-circular (C2C) solar-sail transfers?
   (a) How does an indirect shooting-method compare against a state-of-the-art direct collocation solver (e.g., GPOPS-II) in terms of convergence robustness, computational cost, and solution accuracy for single-revolution transfers?
   (b) How do key sail performance parameters and orbital geometry affect the existence, uniqueness, and performance (defined here as radius gain) of the optimal C2C solution?

3

Journal Article

Indirect Optimization of Planetocentric Solar-Sail Trajectories for Circular Orbit Transfers

Oskar Miller*, Fernando Gámez Losada†, and Jeannette Heiligers‡
Delft University of Technology, Delft, The Netherlands, 2628CD

This paper develops an indirect optimization framework for planetocentric circular-to-circular solar-sail transfers using Pontryagin's Maximum Principle. The formulation is general and applicable to any planet, with numerical results presented for Earth-centered transfers. The optimal control problem is reduced to a two-point boundary value problem solved via single-shooting. Assuming an ideal sail, planar motion, and point-mass gravity (neglecting eclipses and third-body effects), the study yields three main findings. First, transfer performance, measured as final-radius gain for a given transfer duration, strongly depends on the "start-phase" (timing of departure relative to the Sun's apparent motion). Optimal performance occurs when the Sun-line is parallel to the projection of the orbital angular momentum onto the ecliptic at transfer midpoint, whereas worst performance arises when it is perpendicular. This phasing effect dominates high-inclination transfers and becomes negligible at 0° inclination due to constant illumination. Second, dimensional analysis collapses the parameter space into three independent dimensionless groups. Numerical exploration reveals robust power-law scaling of transfer performance with these groups, enabling accurate extrapolation of results across sail designs and initial altitudes from a single benchmark optimization. Third, detailed investigation of the single-shooting solver shows wide convergence basins and smooth solution dependence on orbital parameters, sail characteristics, and transfer duration. Convergence is notably easier for longer transfers and higher ecliptic inclinations, whereas low-inclination, short-duration cases remain the most challenging. The proposed indirect optimization method is therefore demonstrated to be robust, efficient, and suitable for systematic performance mapping of planetocentric solar-sail orbit raising.

I. Introduction

Solar sailing is a propellant-free spacecraft propulsion method that utilizes the momentum carried by sunlight. Rather than burning fuel, solar sailing employs a large, lightweight, highly reflective membrane to convert photon

*M.Sc student, Aerospace Engineering,
†Ph.D. candidate, Astrodynamics and Space Missions. ‡Associate Professor,
Astrodynamics and Space Missions.

pressure into continuous thrust. Since solar sailing requires no propellant, it is an attractive option for long-duration, high-energy mission scenarios [1]. Since the IKAROS mission in 2010 [2], significant practical demonstrations have occurred, which have popularized solar sailing as a technology. In 2019, the Planetary Society's LightSail 2 mission demonstrated controlled solar sailing in Earth orbit, raising orbital altitude purely via solar radiation pressure [3]. With the successful launch and deployment of the NASA Advanced Composite Solar Sail System (ACS3) in early 2024, solar sailing is slowly maturing into a fully accepted form of low-thrust propulsion [4].

While the majority of solar sail research has historically focused on heliocentric trajectories [5–8], there is increasing interest in planetocentric applications. These can be broadly divided into *open-ended* trajectories, which do not terminate in a prescribed bound orbit (e.g., escape, station-keeping, or long-term orbit raising), and *orbit-to-orbit* transfers, in which the spacecraft starts and ends in well-defined bound orbits around the same primary. Open-ended trajectories have been studied extensively [9–13]. By contrast, relatively few studies have investigated planetocentric orbit-to-orbit transfers or rendezvous trajectories, and the studies that do address orbital transfers primarily emphasize mission-specific applications [14–16]. Thus, a general characterization of orbit-to-orbit transfers remains limited.

For planetocentric missions, the low control authority of the solar sail, combined with rapidly changing illumination angles and periodic eclipses, presents a significant challenge. To achieve meaningful orbital changes, the sail must complete many revolutions, resulting in a complex, high-dimensional trajectory optimization problem. Various optimal control methods have been explored to solve many-revolution transfers. Locally optimal control laws are computationally efficient, explaining their widespread use [9–11, 17, 18], but they do not guarantee global optimality. Recent advancements in computational power and algorithms have increased interest in optimal control theory methods, including indirect and direct approaches [15, 19–21]. In terms of orbit-to-orbit transfers, direct methods and differential dynamic programming (DDP) have been successfully used to solve circular-to-circular (C2C) planetocentric orbit transfers [22, 23].

Direct optimization methods transcribe the problem into a large Nonlinear Program (NLP), which is robust but scales poorly with the number of revolutions [24]. Indirect optimization methods leverage the Calculus of Variations and Pontryagin's Maximum Principle (PMP) to reduce the optimal control problem into a finite-dimensional Two-Point Boundary Value Problem (TPBVP). The size of this TPBVP is fixed and independent of the transfer duration, which makes it theoretically attractive for many-revolution transfers [25, 26]. There are limitations to this approach, however, with the indirect method being sensitive to the initial guess of the costates, which has historically limited its practical application [24]. The present work adds a comprehensive theoretical characterization of C2C planetocentric solar sail transfers using indirect optimal control methods and further examines the sensitivity and convergence behavior of the solution process, addressing one of the key challenges historically associated with indirect methods.

This work develops and applies a robust indirect optimization framework to solve the planar, planetocentric solar sail C2C transfer problem. The formulation and methodology are general and apply to C2C transfers around any

planet, while example cases presented in this paper focus on Earth for illustration and validation. A parametric study is performed to derive fundamental insights into the C2C transfer problem. First, the effect of transfer phasing (the start time of the transfer relative to the year of the primary) is analyzed in terms of transfer performance which is defined as radius gain over a given transfer duration. Coupled with the effect of inclination, a transfer envelope is defined for a given transfer duration which defines the minimum and maximum possible radius increase given a transfer time. Second, dimensional analysis is used to form dimensionless groups that allow extrapolation of transfer results across altitudes and values of characteristic sail acceleration. Third, the solver conditioning and convergence are characterized to provide insight into the sensitivity of the indirect method and how to overcome it.

The paper is organized as follows. First, Section II details the methodology, including the dynamical model, the indirect problem formulation, and the dimensional analysis. Second, Section III presents the numerical results, including the phasing analysis and the derivation of the performance extrapolation model. Finally, Section IV analyzes the convergence properties of the numerical method itself.

II. Methodology

In this section, a general description of the reference frames, dynamical model, and coordinate systems is given. Subsequently, the equations of motion (EoM) are presented. After that, the indirect problem formulation is laid out, which forms the basis of the optimization. To conclude, an overview is given of the software and numerical tools used.

A. Reference Frames

The following work makes use of three reference frames, which are described below and shown in Figure 1a. Throughout, the *central body* is referred to as the *primary*.

- **Primary-Centered Inertial (PCI, denoted by $\mathcal{I}_P(X, Y, Z)$):** the PCI frame is centered at the primary's barycenter. The axes are non-rotating relative to the International Celestial Reference Frame (ICRF), with $\hat{X}$ pointing along the first axis of the ICRF (the J2000 vernal equinox direction), $\hat{Z}$ normal to the ecliptic plane at the chosen epoch, and $\hat{Y}$ completing the right-handed triad. The initial epoch is taken as t_0 = J2000 for simplicity.
- **Sunlight Fixed (SLF, denoted by $\mathcal{S}(x, y, z)$):** the SLF frame is centered at the spacecraft position, with the $\hat{x}$ axis parallel to the Sun-line, $\hat{s}$ (from the Sun to the spacecraft), the $\hat{z}$ axis parallel to the $\hat{Z}$ direction of $\mathcal{I}_P$, and $\hat{y}$ completing the right-handed frame. The SLF frame is mainly used to define the sail orientation.
- **Radial–Tangential–Normal (RTN, denoted as $\mathcal{O}(R, T, N)$):** the RTN frame is centered at the spacecraft position, with the $\hat{R}$ axis directed radially away from the primary, the $\hat{N}$ axis parallel to the orbital angular momentum vector, $\hat{h}$, and the $\hat{T}$ axis completing the right-handed frame. The RTN frame provides a convenient basis for formulating the local dynamics in polar coordinates.

Throughout this work, subscripts are used to indicate the reference frame associated with a vector. For rotation

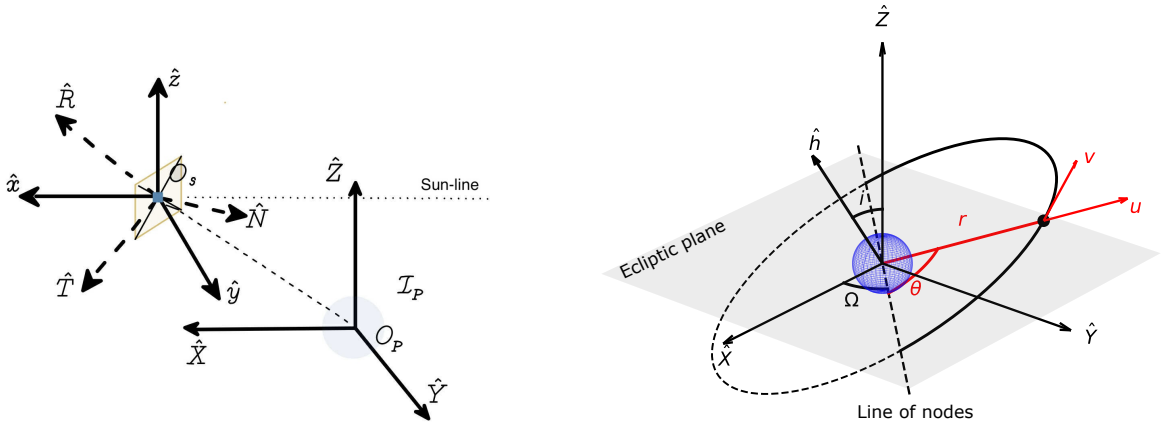

(a) PCI, SLF, and RTN frames. **(b) The polar coordinate system**

Fig. 1 Reference frames and coordinate system representation

matrices, the subscript denotes the original (source) frame, while the superscript denotes the target frame. For example, $\boldsymbol{q}_S = R_O^S \boldsymbol{q}_O^{\mathrm{T}}$ represents the transformation of the vector $\boldsymbol{q}$ from the RTN frame to the SLF frame.

B. Dynamical Model

In this study, the motion of the solar sail about a primary is described accounting only for point-mass gravity and the solar-sail acceleration, which is modeled using an ideal solar sail [1]. Non-ideal effects (e.g., imperfect reflectivity, absorption and thermal re-emission, membrane wrinkling, and structural deformations), eclipses, and perturbing forces (e.g., non-spherical gravity and aerodynamic drag) are neglected for simplicity but should be considered in future work because they have been shown to significantly impact sail performance [27, 28]. The Sun is assumed to be infinitely far away from the primary which means that incoming radiation is assumed to be parallel to the Sun-line $\hat{x}$.

The circular-to-circular (C2C) transfer is modeled as a two-dimensional (2D) motion confined to the orbital plane. The out-of-plane component of the solar-sail acceleration is therefore neglected, and only the in-plane component is included in the EoM. Because the solar-sail acceleration is small in magnitude and the control profile is periodic, the resulting out-of-plane motion during the transfer would remain negligible.

The orientation of the solar sail can be represented in different ways. A common representation is the cone–clock angle pair (α and δ, respectively). The cone angle α is the angle between the Sun-line and the sail normal vector, defining the illumination conditions of the sail. The clock angle δ defines the sail's azimuthal orientation around the Sun-line and is measured in the SLF frame about the $+\hat{x}$-axis, with $\delta = 0$ aligned with $+\hat{z}$ and increasing toward $+\hat{y}$. The acceleration vector $\mathbf{a}_S$ (defined in SLF) is then defined as:

$$\boldsymbol{a}_S = a_0 \cos^2\alpha \left[\cos\alpha,\ \sin\alpha\sin\delta,\ \sin\alpha\cos\delta\right]^{\mathrm{T}} \tag{1}$$

where a_0 is the solar-sail characteristic acceleration at an average distance between the primary and the Sun. When deriving the dynamics, the solar-sail acceleration will mainly appear in the RTN frame with a_R denoting the acceleration in the radial direction and a_T denoting the acceleration in the tangential direction.

The sail performance can be described as a function of its maximum acceleration magnitude at the primary's heliocentric distance and the sail orientation. The orbit of the primary around the Sun is assumed to be circular, which means that the heliocentric distance of the primary is constant. This assumption implies a constant characteristic acceleration, and therefore the solar-sail acceleration depends only on the orientation of the sail.

C. Coordinate Systems

The modeled dynamics are constrained to in-plane motion which means that the spacecraft state can be efficiently described using polar coordinates. The coordinate system is shown in Figure 1b. The polar state vector is $\mathbf{x_t} = \begin{bmatrix} r, & \theta, & u, & v \end{bmatrix}$, where r (radius) is the radial distance from the primary, θ (argument of latitude) is the angular position of the spacecraft measured in the orbital plane relative to the line of nodes, u is the radial velocity, and v is the tangential velocity. Additionally, as seen in Figure 1b, the inclination, i, is defined as the angle between the angular momentum vector of the orbit, $\hat{h}$, and the inertial $\hat{Z}$-axis and the right ascension of the ascending node (RAAN), Ω, is defined as the angle between the inertial $\hat{X}$-axis and the line of nodes.

To improve numerical stability, an alternative formulation is introduced in which the independent variable is transformed from time t to the accumulated anomaly θ using a Sundman transform [29]. After the transformation, the state vector becomes $\mathbf{x}_\theta = \begin{bmatrix} r, & t, & u, & v \end{bmatrix}$. In this formulation, the transfer duration is specified in terms of the total angular displacement from the initial position, denoted here as the argument of latitude.

The use of argument of latitude as the independent variable instead of time is advantageous because the control laws in this work appear to be periodic with the orbital period. By specifying the transfer duration as an integer number of revolutions, the trajectory begins and ends at the same angular location, which reduces discontinuities and improves convergence. By contrast, when the transfer duration is specified in seconds, the endpoint often falls mid-orbit, complicating the numerical solution.

D. Scaling

The EoM describing the dynamics of the OCP are normalized to order unity to improve numerical stability and convergence properties. The scaled parameters are:

$$\bar{t} = \frac{t}{t_f}, \quad \bar{r} = \frac{r}{r_0}, \quad \bar{\theta} = \frac{\theta}{\theta_f}, \quad \bar{u} = \frac{u}{v_0}, \quad \bar{v} = \frac{v}{v_0}, \tag{2}$$

where t_f is the time of flight, r_0 is the initial radius, θ_f is the argument of latitude at the final time, and v_0 is the initial velocity. The scaled EoM with time as the independent variable can be seen in Eq. (3), and the scaled EoM with argument of latitude as the independent variable can be seen in Eq. (4).

$$\begin{cases} \dfrac{d\bar{r}}{d\bar{t}} = \bar{u}\dfrac{v_0 t_f}{r_0}, \\ \dfrac{d\bar{\theta}}{d\bar{t}} = \dfrac{\bar{v}}{\bar{r}}\dfrac{v_0 t_f}{r_0\theta_f}, \\ \dfrac{d\bar{u}}{d\bar{t}} = \left(\dfrac{\bar{v}^2}{\bar{r}} - \dfrac{1}{\bar{r}^2}\right)\dfrac{v_0 t_f}{r_0} + a_R\dfrac{t_f}{v_0}, \\ \dfrac{d\bar{v}}{d\bar{t}} = -\dfrac{\bar{u}\bar{v}}{\bar{r}}\dfrac{v_0 t_f}{r_0} + a_T\dfrac{t_f}{v_0}. \end{cases} \tag{3}$$

$$\begin{cases} \dfrac{d\bar{r}}{d\bar{\theta}} = \dfrac{\bar{u}\bar{r}}{\bar{v}}\theta_f, \\ \dfrac{d\bar{t}}{d\bar{\theta}} = \dfrac{\bar{r}}{\bar{v}}\dfrac{\theta_f r_0}{v_0 t_f}, \\ \dfrac{d\bar{u}}{d\bar{\theta}} = \left(\bar{v} - \dfrac{1}{\bar{r}\bar{v}}\right)\theta_f + a_R\dfrac{\bar{r}}{\bar{v}}\dfrac{r_0\theta_f}{v_0^2}, \\ \dfrac{d\bar{v}}{d\bar{\theta}} = -\bar{u}\theta_f + a_T\dfrac{\bar{r}}{\bar{v}}\dfrac{r_0\theta_f}{v_0^2}. \end{cases} \tag{4}$$

In the following work, all problems will be formulated and solved with argument of latitude as the independent variable unless stated otherwise. This choice is made due to the convergence benefits of being able to define the transfer duration as integer number of revolutions. Thus, in following work, the $\dot{\square}$ notation means derivative with reference to the argument of latitude.

E. Indirect Problem Formulation

In this subsection, the indirect OCP together with TPBVP will be formulated based on the dynamics derived in Section II.D.

1. Optimal control problem

The objective of the planar C2C solar sail transfer is to maximize the radius change over a given transfer duration while keeping the terminal orbit circular [22, 23]. Thus:

$$\text{minimize} \quad \mathcal{J} = -\bar{r}_f, \tag{5a}$$

subject to

$$\dot{\boldsymbol{x}} = \text{Eq. (4)}, \tag{5b}$$

$$\boldsymbol{x}_0 = \begin{bmatrix} 1 & 0 & 0 & 1 \end{bmatrix}^T, \tag{5c}$$

$$\boldsymbol{\Psi} = \begin{pmatrix} \bar{u}_f \\ \bar{v}_f - \dfrac{1}{\sqrt{\bar{r}_f}} \end{pmatrix} = \boldsymbol{0}, \tag{5d}$$

where $\mathcal{J}$ is the objective function, the sub-index f indicates values at the final epoch, $\dot{x}$ is the argument of latitude derivative of the state, and Ψ is the terminal function. $\boldsymbol{x}_0$ sets the initial orbit to be circular and $\boldsymbol{\Psi}$ requires the terminal orbit to be circular, completing the C2C transfer. In the following work, the transfer performance $\mathcal{P}$ is defined as the scaled radius gain over the given transfer duration: $\mathcal{P} = r_f/r_0 - 1$.

2. Hamiltonian and the Pontryagin's Maximum Principle

The Hamiltonian is defined as:

$$\begin{aligned} H &= \boldsymbol{\lambda}^T \boldsymbol{f}(t, \boldsymbol{x}, \boldsymbol{u}) \\ &= \lambda_{\bar{r}} \cdot \frac{\bar{u}\bar{r}}{\bar{v}}\theta_f + \lambda_{\bar{t}} \cdot \frac{\bar{r}}{\bar{v}}\frac{\theta_f r_0}{v_0 t_f} + \lambda_{\bar{u}} \cdot \left[\left(\bar{v} - \frac{1}{\bar{r}\bar{v}}\right)\theta_f + a_R\frac{\bar{r}}{\bar{v}}\frac{r_0\theta_f}{v_0^2}\right] + \lambda_{\bar{v}} \cdot \left[-\bar{u}\theta_f + a_T\frac{\bar{r}}{\bar{v}}\frac{r_0\theta_f}{v_0^2}\right], \end{aligned} \tag{6}$$

where $\boldsymbol{\lambda} = \begin{bmatrix} \lambda_{\bar{r}}, & \lambda_{\bar{t}}, & \lambda_{\bar{u}}, & \lambda_{\bar{v}} \end{bmatrix}^T$ is the costate vector with costates related to $\bar{r}$, $\bar{t}$, $\bar{u}$, and $\bar{v}$ respectively, $\boldsymbol{f}$ is the system dynamics given by Eq. (4), and $\boldsymbol{u}$ is the control-input vector. Pontryagin's maximum principle (PMP) states that the optimal control input minimizes the Hamiltonian at each point along the trajectory. The part of the Hamiltonian that depends on the control can be written as $\mathcal{H}$:

$$\mathcal{H} = \frac{\bar{r}}{\bar{v}}\frac{r_0\theta_f}{v_0^2}\begin{bmatrix} \lambda_{\bar{u}}, & \lambda_{\bar{v}}, & 0 \end{bmatrix}\begin{bmatrix} a_R \\ a_T \\ a_N \end{bmatrix}. \tag{7}$$

Equation (7) shows that, to minimize the Hamiltonian at every time step, the control must be chosen such that the acceleration is minimized in the $\begin{bmatrix} \lambda_{\bar{u}}, & \lambda_{\bar{v}}, & 0 \end{bmatrix}$ direction or, alternatively, maximized in the $\begin{bmatrix} -\lambda_{\bar{u}}, & -\lambda_{\bar{v}}, & 0 \end{bmatrix}$ direction. The direction in which the acceleration must be maximized is also called the primer vector direction. Ref. [1] gives the analytical formulation of the cone and clock angles to maximize the projection of the acceleration in a certain direction:

$$\boldsymbol{q}_O = \begin{bmatrix} -\lambda_{\bar{u}} & -\lambda_{\bar{v}} & 0 \end{bmatrix},$$

$$\boldsymbol{q}_S = R_O^S \boldsymbol{q}_O^{\mathrm{T}},$$

$$\phi = \tan^{-1}\left(\frac{\left\|\boldsymbol{q}_S \times \hat{\boldsymbol{x}}\right\|}{\boldsymbol{q}_S^{\mathrm{T}} \hat{\boldsymbol{x}}}\right),$$

$$\alpha = \frac{1}{2}\left[\phi - \sin^{-1}\left(\frac{\sin\phi}{3}\right)\right],$$

$$\delta = \tan^{-1}\left(\frac{\boldsymbol{q}_y}{\boldsymbol{q}_z}\right),$$

where $\boldsymbol{q}$ denotes the primer vector, and R_O^S is the rotation matrix that transforms quantities from the RTN frame to the SLF frame. The solar-sail acceleration in the SLF frame, $\boldsymbol{a}_S$, is defined by Eq. (1). To obtain the radial and transverse acceleration components, a_R and a_T, the acceleration vector must be transformed back to the RTN frame:

$$\boldsymbol{a}_O = R_S^O \boldsymbol{a}_S^{\mathrm{T}}.$$

As a result of applying the PMP to derive the primer vector direction, and using the analytical relationship provided in Ref. [1] to relate the primer vector to the cone and clock angles, the control can be expressed directly as a function of the costates. This formulation removes the need to treat the control as an explicit parameter in the problem definition.

3. Euler-Lagrange Equations

The Euler-Lagrange Equations define the dynamics of the costates:

$$\dot{\boldsymbol{\lambda}} = -\frac{\partial H}{\partial \boldsymbol{x}}. \tag{8}$$

The partial derivatives with reference to $\bar{r}$, $\bar{u}$, and $\bar{v}$ can be derived analytically. However, the partial derivative involving time is considerably more complex because the calculation of the solar-sail acceleration components, a_R and a_T, includes time through the orbit of the primary around the Earth. Thus, time appears in the rotation matrix used in the primer-vector calculation which is makes the analytical expressions complex. To handle the complex expressions efficiently and ensure exact derivatives, automatic differentiation with JAX is used instead [30]. Automatic differentiation provides numerically precise gradients, keeps the implementation consistent with the Hamiltonian definition, and avoids the need for manual symbolic differentiation of the nested rotation terms. With the dynamics of the costates known, they can be integrated together with the state vector. Additionally, the control is written through the costates, which means that the full control profile throughout the transfer is defined by the initial values of the four costates.

4. Terminal Function

The terminal function is given by:

$$\Phi = \phi + \boldsymbol{\nu}^T \boldsymbol{\Psi} = -\bar{r}_f + \nu_1 \bar{u}_f + \nu_2 \left(\bar{v}_f - \frac{1}{\sqrt{\bar{r}_f}} \right), \tag{9}$$

where ϕ is the terminal cost, $\boldsymbol{\nu} = \begin{bmatrix} \nu_1, & \nu_2 \end{bmatrix}^T$ is the vector of Lagrange multipliers, and $\boldsymbol{\Psi}$ is the terminal constraint vector from Equation (5d). From Eq. (9), the terminal boundary conditions for the costates can be derived as $\boldsymbol{\lambda}(1) = \partial\Phi/\partial \boldsymbol{x}$ [26] and expand as follows:

$$\begin{aligned} \lambda_{\bar{r}}(1) &= \frac{\partial \Phi}{\partial \bar{r}} = -1 + \frac{1}{2}\nu_2 \left(\bar{r}_f\right)^{-\frac{3}{2}}, \\ \lambda_{\bar{t}}(1) &= \frac{\partial \Phi}{\partial \bar{t}} = 0, \\ \lambda_{\bar{u}}(1) &= \frac{\partial \Phi}{\partial \bar{u}} = \nu_1, \\ \lambda_{\bar{v}}(1) &= \frac{\partial \Phi}{\partial \bar{v}} = \nu_2. \end{aligned} \tag{10}$$

The terminal costates describe how sensitive the optimal value of the cost functional (performance index) is to small changes in the terminal state variables. In other words, they represent the marginal cost or value of relaxing or tightening the terminal constraints at the final time.

First, the terminal radial costate $\lambda_{\bar{r}}$ in Eq. (10) shows a trade-off between the objective and the circularity constraint. The term -1 originates from the performance index, reflecting the fact that increasing the final radius directly improves the objective. The correction $\frac{1}{2}\nu_2 \left(\bar{r}_f\right)^{-\frac{3}{2}}$ accounts for the coupling to the circular velocity requirement $\bar{v}_f = \frac{1}{\sqrt{\bar{r}_f}}$. Hence $\lambda_{\bar{r}}(1) < 0$ when radius gain dominates, $\lambda_{\bar{r}}(1) = 0$ at balance, and $\lambda_{\bar{r}}(1) > 0$ when maintaining circularity at larger radius is marginally costly.

Secondly, the terminal costates associated with velocity satisfy $\lambda_{\bar{u}}(1) = \nu_1$ and $\lambda_{\bar{v}}(1) = \nu_2$, showing that the Lagrange multipliers are exactly the sensitivities of the augmented terminal cost to small violations of the terminal radial and tangential velocity constraints. Furthermore, $[-\nu_1, -\nu_2]$ are the terminal components of the primer vector, determining the final thrust orientation in the orbital plane.

5. Two-Point Boundary Value Problem

There are four states, four costates, and two Lagrange multipliers. The eight differential equations from Eq. (4) and Eq. (8), together with the eight boundary conditions from Eq. (5c) and Eq. (10), define a TPBVP. The multipliers $\boldsymbol{\nu}$ are chosen so that the two algebraic side conditions in Eq. (5d) are satisfied. Equivalently, the final formulation is a TPBVP with eight coupled first-order ODEs and two algebraic constraints that must be solved simultaneously to obtain the optimal sail orientations.

To formalize the boundary-value problem, the unknowns of the indirect formulation are collected into a single solution vector. Let the vector of the free initial costates be noted by:

$$\boldsymbol{\Lambda_0} = \left[\lambda_{\bar{r}}(0),\ \lambda_{\bar{t}}(0),\ \lambda_{\bar{u}}(0),\ \lambda_{\bar{v}}(0)\right]^T. \tag{11}$$

The complete vector of unknowns is then defined as:

$$\boldsymbol{w} = \left[\boldsymbol{\Lambda_0},\ \boldsymbol{\nu}\right]. \tag{12}$$

The TPBVP can be written compactly in terms of a residual function:

$$\boldsymbol{F}(\boldsymbol{w}) \in \mathbb{R}^6. \tag{13}$$

For any trial value of $\boldsymbol{w}$, the coupled state-costate ODEs in Eq. (4) and Eq. (8) are integrated from the normalized argument of latitude 0 to 1. At the terminal point, six scalar residuals are assembled based on Eq. (10) and Eq. (5d). The TPBVP is equivalent to the nonlinear root-finding problem:

$$\boldsymbol{F}(\boldsymbol{w}^*) = \boldsymbol{0}. \tag{14}$$

F. Software and Numerical Implementation

All numerical experiments were implemented in Python using JAX for high-performance array computations and automatic differentiation [30], Diffrax for adaptive ordinary differential equation (ODE) integration [31], and two root-finding back ends: SciPy's `fsolve` and `jaxopt.ScipyRootFinding` [32][33].

1. Problem structure

The indirect formulation is solved by single shooting. For a given guess of the four initial costates and two terminal Lagrange multipliers, the state–costate ODEs are integrated from the normalized independent variable 0 to 1. At the endpoint, the two terminal dynamics constraints (circular orbit) and the four transversality conditions (costate equal to the gradient of the terminal function) are assembled into a six-component residual; a root of this residual yields the optimal $\boldsymbol{w}$.

2. Ordinary differential equation integration

The initial value problems are integrated with Diffrax's explicit eighth-order Runge–Kutta method (`Dopri8`) and a `PIDController` for step-size adaptation [34]. The ODE solver tolerances were set to `rtol` = 10^{-12} and `atol` = 10^{-12} so that numerical integration errors are negligible compared to the modeling uncertainties. Tight tolerances are feasible

with double-precision arithmetic, and spot checks with stricter tolerances (an order of magnitude smaller) produced changes in the final performance index and terminal state well below 10^{-8} relative, indicating that the chosen settings are sufficient for the present study. All performance-critical functions (rotation matrices, control law from the primer vector, state dynamics, Hamiltonian gradient, terminal residuals) are just-in-time-compiled with `jax.jit`. To differentiate the Hamiltonian with respect to the state, `jax.grad` is applied to a scalar Hamiltonian; the costate dynamics are then $-\partial H/\partial \boldsymbol{w}$ as in the formulation.

3. Root finding

Two interchangeable drivers were used to solve the six-dimensional nonlinear system for $\boldsymbol{w}$:

1) **SciPy `fsolve`** (MINPACK hybrid method). The $d\boldsymbol{F}/d\boldsymbol{w}$ is not supplied, which means that it is formed by finite differences.
2) **`jaxopt.ScipyRootFinding`**. This function wraps the same MINPACK algorithm but supplies Jacobian information using JAX. Jacobians are computed in *forward-mode* automatic differentiation.

The root-finding tolerance was set to `tol` = 10^{-10}, which ensures that the residuals of the two-point boundary value problem are driven to a level where the remaining error is dominated by modeling assumptions rather than numerical inaccuracies. The detailed implementation is available upon request.

III. Numerical Results

This section focuses on the performance, defined as the radius change over the given transfer duration, of the planar planetocentric C2C solar sail transfers and its relation to problem parameters. Section III.A describes the importance of phasing the transfer by looking at the effect of the orientation of the orbital plane with reference to the Sun-line on transfer performance. Section III.B analyzes the effect of Π-groups that will be defined in Section III.B.1 on transfer performance and proposes a scaling model to extrapolate transfer performance between different sail designs and initial orbital configurations.

A. Transfer Phasing Function

The solar sail transfers are generally long duration due to the solar-sail acceleration being small in magnitude, which means that it will take many revolutions to raise or lower the orbit to the target altitude. During the transfer, the primary moves around the Sun, which means that the Sun-line is constantly moving with reference to the orbital plane of the spacecraft. To define the illumination conditions of the orbital plane, the aspect angle (AA) can be used, which is defined as the angle between the Sun-line and the orbit's angular momentum vector. For one-revolution transfers, where the Sun-line can be assumed to be fixed (transfer duration is small compared to the length of the primary's year), the performance is worst when $AA = 90°$ and best when $AA = 0°$ [22].

For many-revolution transfers, however, the rotation of the Sun-line around the orbital plane must be taken into account. Over the course of the primary's year, the Sun-line completes one full rotation relative to the orbit, causing the aspect angle to vary periodically with the same period. The resulting AA profile describes how the aspect angle evolves with time during this annual cycle. Its shape depends on the inclination and orientation of the orbit relative to the ecliptic: low-inclination orbits experience small oscillations of AA around 90°, whereas high-inclination orbits can exhibit large variations ranging from near 0° to 180°.

When the duration of the transfer does not span exactly one year, the spacecraft samples only a portion of the yearly AA profile. The transfer duration effectively defines a "slice" of the annual variation that determines the illumination conditions experienced during the maneuver. Phasing the start of the transfer then corresponds to selecting the initial point of this slice along the yearly AA cycle, allowing the start time to be optimized so that the AA profile over the transfer duration is as favorable as possible and the orbital radius change is maximized.

To parameterize phasing, the start-phase, γ_0, can be defined as:

$$\gamma_0 \equiv \Omega - L_s\left(t_0\right), \tag{15}$$

where $L_s\left(t_0\right)$ is the solar longitude (i.e., the position of the Sun on the celestial sphere along the orbital plane of the primary) at the start of the transfer. In all the analysis, the initial solar longitude is set to $L_s\left(t_0\right) = 0$, which means that the start-phase is equivalent to the RAAN. The effect of the start-phase on transfer performance, $\mathcal{P}$, defined here as the radius gain scaled by the initial radius, is shown in Figure 2. The figure shows the transfer performance, $\mathcal{P}$, as a function of the start-phase, γ_0, for a quarter-year transfer ($t_f = 0.25$ years) for inclination values of $i = [0°, 30.0°, 60.0°, 90.0°]$. The chosen scenario corresponds to a GEO-altitude orbit ($r_0 = 42164$ km) and an ACS3-like solar sail ($a_0 = 0.05$ m/s^2).

Two trends emerge in Figure 2. Firstly, the transfer performance follows a periodic trend with reference to the start-phase. The largest radius gain happens when the start-phase is approximately $\gamma_0 \approx 135°$ and $\gamma_0 \approx 315°$, and the smallest radius gain happens when the start-phase is 90° shifted from the optimal phase: at $\gamma_0 \approx 45°$ and $\gamma_0 \approx 225°$. For a 0.25-year transfer, the solar longitude goes from $L_s = 0°$ at the origin to $L_s = 90°$ (a quarter of a full circle). At the start-phase of $\gamma_0 = 135°$, the projection of the angular momentum vector of the orbit onto the ecliptic plane of the primary is pointing in the $L_s = 45°$ direction. With the Sun-line rotating at a uniform rate, the Sun-line and the projection of the angular momentum vector are parallel at exactly the midpoint of the transfer. For the worst-phased scenario of $\gamma_0 = 225°$, the angular momentum vector is pointing in the $L_s = 135°$ direction, which means that the Sun-line and the angular momentum vector are perpendicular to each other at the midpoint of the transfer. This pattern shows that the highest transfer performance is observed when, at the midpoint of the transfer, the Sun-line and the orbit's angular momentum vector projected onto the ecliptic plane are parallel. Performance is worst when the start-phase is rotated by 90° from this optimal phase, when those two vectors are exactly perpendicular at the transfer's halfway point.

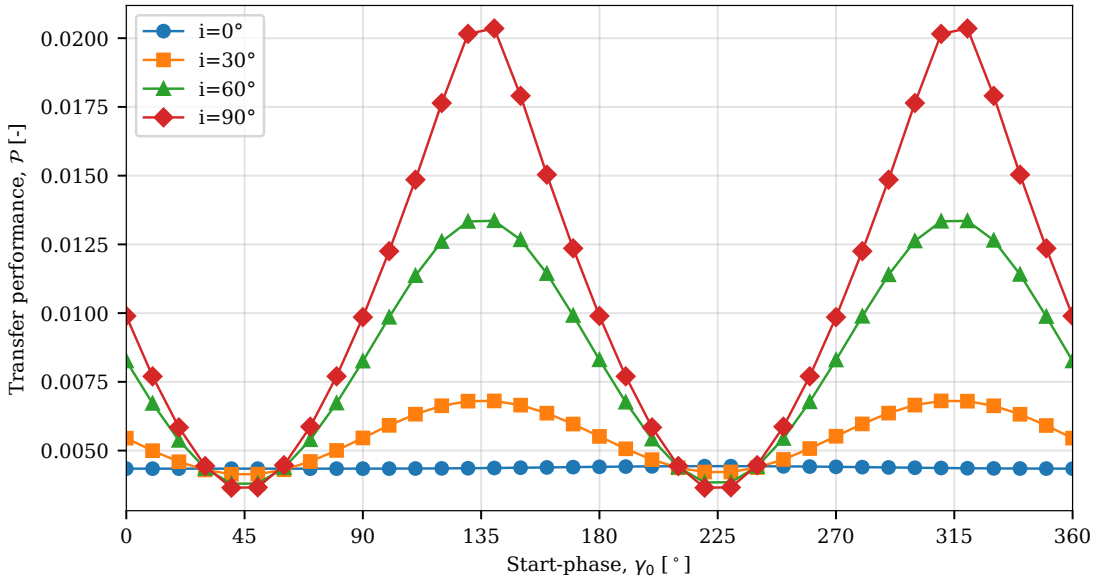

Fig. 2 Transfer performance $\mathcal{P}$ as a function of the start-phase γ_0: $i = [0°, 30.0°, 60.0°, 90.0°]$, $t_f = 0.25$ yr, $a_0 = 0.05$ m/s^2, $r_0 = 42164$ km.

These findings are consistent with the semi-analytical findings of Gámez Losada et al. [35]. To formalize the phasing law, the best and worst start-phase can be defined as:

$$\gamma_0^{\text{best}} \equiv \frac{\omega t_f}{2} + \frac{\pi}{2} \pmod{\pi}, \tag{16}$$

$$\gamma_0^{\text{worst}} \equiv \frac{\omega t_f}{2} \pmod{\pi}, \tag{17}$$

where ωt_f is the angular sweep that the Sun-line makes during the transfer.

The second trend that can be noted in Figure 2 is that the difference between the best and worst phasing is strongly dependent on the inclination of the initial orbit. The largest difference between best- and worst-phased transfer performance happens at an inclination of $i = 90°$, while the smallest difference happens at an inclination of $i = 0°$. At 0° inclination, the Sun-line lies in the orbital plane at all possible solar longitude values, which means that, throughout the transfer, the AA is constant and equal to 90° and phasing has a negligible effect. As inclination increases, the possible variation in AA also increases and thus, phasing becomes more important.

To illustrate the reason behind the performance difference between best and worst phasing, the eccentricity profiles of best- and worst-phased 0.5-year transfers ($r_0 = 42164$ km, $a_0 = 0.05$ mm/s^2) with an inclination of $i = 90°$ are shown in Figure 3. The eccentricity vector is defined in the PCI frame with direction pointing from apoapsis to periapsis and with length equal to the scalar eccentricity of the orbit. Additionally, schematics of the same transfers are shown in

Figure 4 with transfer arcs coloured based on which way the orbit-growth is happening: green if in the $-\hat{Z}$ direction and red if in the $+\hat{Z}$ direction.

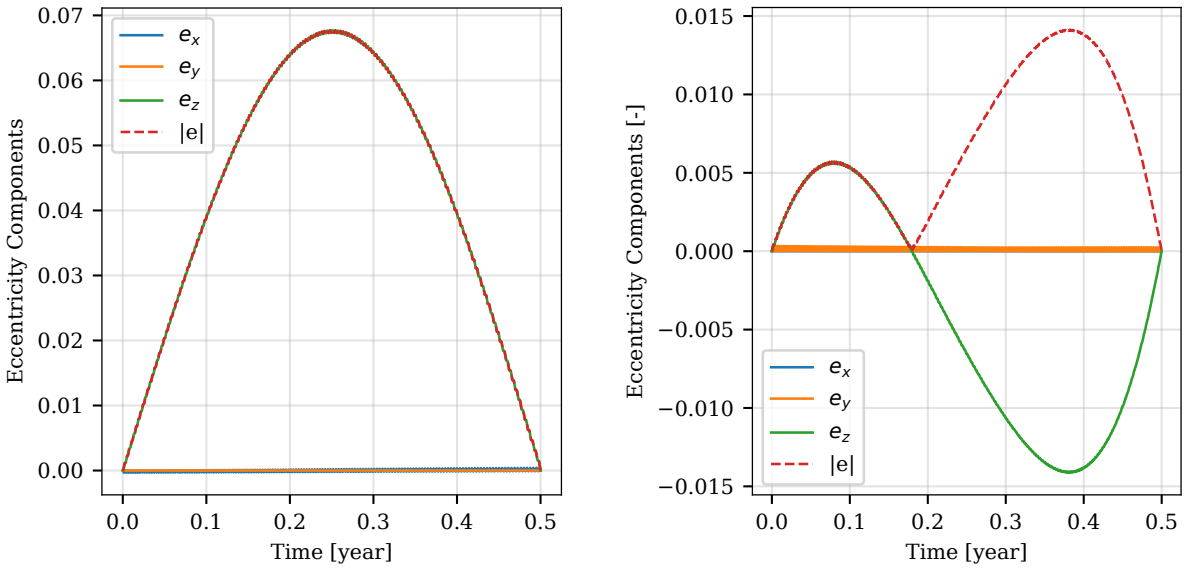

(a) (b)

Fig. 3 Eccentricity vector components and magnitude of 0.5-year transfers with an inclination of $i = 90°$: a) best phasing and b) worst phasing. $r_0 = 42164$ km, $a_0 = 0.05$ mm/s^2

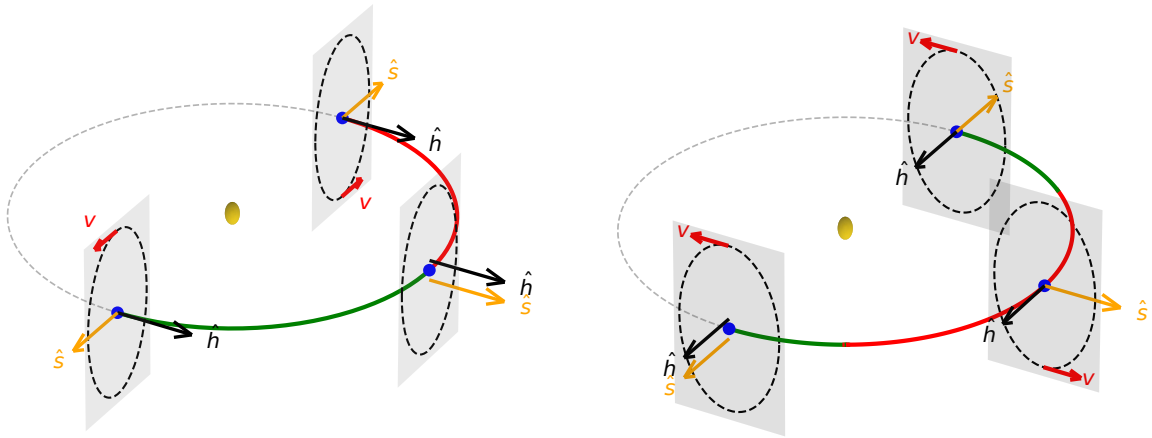

(a) (b)

Fig. 4 Schematics of 0.5-year transfers with an inclination of $i = 90°$: a) best phasing and b) worst phasing. Green arcs indicate apoapsis growth in the $-\hat{Z}$ direction and red arcs indicate apoapsis growth if in the $+\hat{Z}$ direction.

The best-phased transfer, in Figure 3a, initially grows the apoapsis in the negative $\hat{Z}$-direction. This direction of growth is favored by the fact that, due to the counterclockwise movement of the sail around the primary, the sail is

moving away from the Sun on the positive $\hat{Z}$ side of the orbit as seen in the first epoch of Figure 4a, which means that it is optimal to thrust tangentially and grow the apoapsis on the other side. At the halfway point of the transfer the apoapsis growth direction changes. The Sun-line and the angular momentum vector cross, and the sail is moving away from the Sun on the negative $\hat{Z}$ side of the orbit, which allows for efficient circularization of the orbit in the second half of the transfer.

The worst-phased transfer, in Figure 3b, shows a very different eccentricity profile. It can be seen that in the first part of the transfer, the sail grows the apoapsis in the negative $\hat{Z}$-direction just as in the best-phased transfer. Then, it starts circularizing the orbit and growing the apoapsis in the opposite direction. For the last quarter of the transfer, the direction is again switched and the orbit is finally circularized. It is visible from Figure 4b that for the whole transfer duration, the sail is moving away from the Sun on the negative $\hat{Z}$ side of the orbit. At all times it would be efficient to thrust tangentially on the $\hat{Z}$ side and grow the apoapsis in the positive $\hat{Z}$ direction. However, C2C transfers require symmetric growth of the orbit in both directions and the optimizer is forced to place the less efficient negative $\hat{Z}$ orbit-raising segments at the beginning and end of the maneuver, where their impact on overall performance is minimized.

Due to the existence of clear best- and worst-cases, and their dependence on transfer duration, a transfer performance envelope can be defined by calculating the best and worst transfer performances for a range of transfer durations while keeping the orbital geometry fixed. Transfer performance envelopes are visualized in Figure 5. The figure shows transfer performance as a function of transfer duration for the best and worst phasing for various values of the ecliptic inclination.

Multiple trends can be noted in Figure 5. First, the size of the envelope increases with inclination, which matches the conclusion from Figure 2. The envelopes are narrower when looking at short-duration transfers, then widen as the duration increases, and finally tighten again as the transfer duration approaches the one-year mark. At short transfer durations, there is not enough time for the phasing to have a significant effect on transfer performance, and at transfer durations of around one year, the sail "witnesses" the full range of AAs no matter the phasing, so the effect is minimal. The envelope is largest when the transfer duration is equal to half a year where, as explained before, the worst transfer only experiences AAs that favor orbit raising in one direction. Once the transfer duration goes beyond that, even the worst-phased transfers have some regions during the transfer where it is favorable to raise the orbit in the opposite direction.

Another interesting observation to note in Figure 5 is the fact that lower inclinations outperform higher inclinations near the one-year duration. Generally, the higher-inclination transfers perform better because they have better illumination conditions (favorable AA profiles), which allow for both orbit raising and circularization. At lower inclinations, the sail could easily raise the orbit every time it is moving away from the Sun, but it is very difficult to circularize because it is hard to increase the orbital energy when moving back towards the Sun on the other side of the orbit. For transfer durations nearing one year, on the other hand, the lower-inclination cases can make use of the symmetry that the full revolution of the Sun-line provides to effectively raise and circularize the orbit.

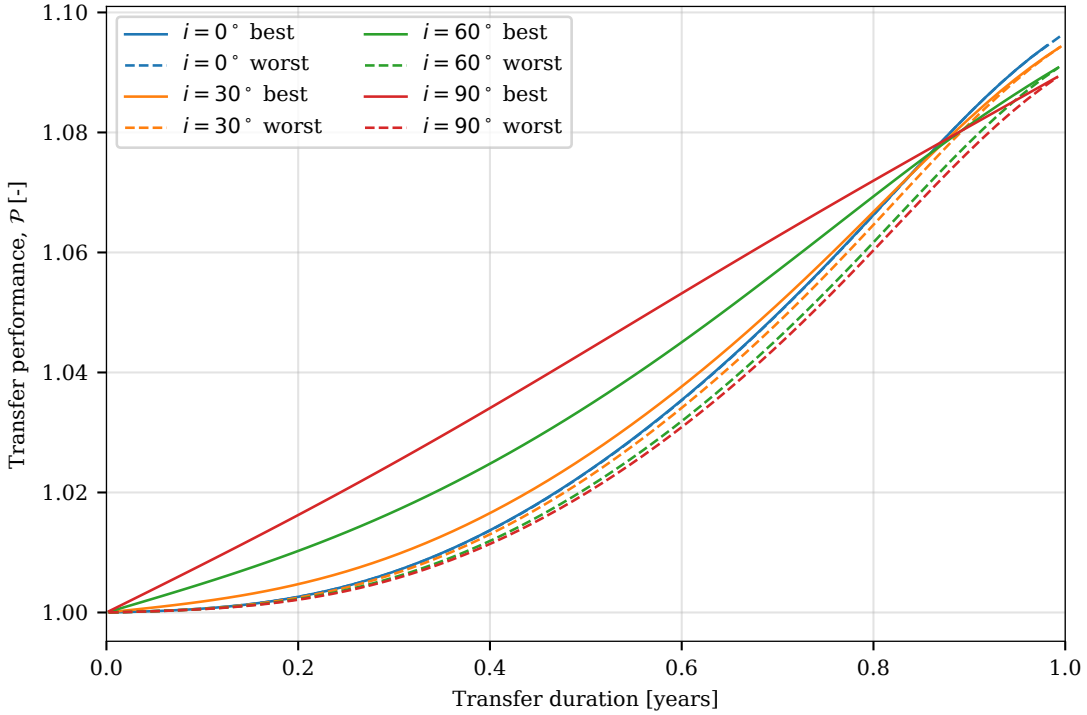

Fig. 5 Transfer performance envelopes for a range of inclination values. r_0 = 42164 km, a_0 = 0.01 mm/s^2

B. Transfer Performance Extrapolation Model

The effect of orbital plane orientation (inclination and RAAN) with respect to the Sun was discussed in Section III.A. In this section, the focus will be on the remaining parameters that are used to define the OCP: r_0, a_0, μ, ω.

1. Dimensional Analysis and Π*-Groups*

The transfer performance depends on a variety of parameters. There are parameters that relate to sail performance, like the characteristic acceleration of the sail, a_0. The orbital geometry is set by inclination, i, RAAN, Ω, and initial radius, r_0. The gravitational parameter, μ, and angular velocity of the primary's orbit around the Sun, ω, define the characteristics of the primary. Finally, the transfer duration is specified by either the final argument of latitude, θ_f, or time, t_f. When designing a mission, it is more useful to specify the transfer duration in time, so this is the formulation that will be discussed in this section. The derived relations remain valid if the argument of latitude is used as the independent variable; however, in that case the final time must be obtained from the state vector at the transfer's final epoch.

The problem has $n = 5$ dimensional inputs (r_0, μ, ω, a_0, t_f) and 2 dimensionless inputs (Ω, i). The base dimension rank is $r = 2$ (length and time). By Buckingham's π theorem [36], the number of independent dimensionless groups, also known as Π-groups, is $n - r = 3$. Two problems with different dimensional inputs but same dimensionless inputs

would then yield the same dimensionless optimal control profiles and trajectories. One could define physically intuitive Π-groups like scaled characteristic acceleration, ξ, Sun-line drift per orbit, $\dot{S}$, and Sun-line drift over transfer, S, as:

$$\xi \equiv \frac{a_0\, r_0^2}{\mu}, \tag{18a}$$

$$\dot{S} \equiv 2\pi\, \omega \sqrt{\frac{r_0^3}{\mu}}, \tag{18b}$$

$$S \equiv \omega\, t_f. \tag{18c}$$

The scaled characteristic acceleration quantifies the sail's strength relative to local gravity at the initial state, while $\dot{S}$ and S quantify the angular advance of the Sun-line during one orbital period and transfer duration, respectively. The upside to this formulation is the physical interpretability, while the downside is that r_0 appears in the definitions of both ξ and $\dot{S}$. When designing a mission, the primary is generally fixed, and the common trade studies are done on the sail design and orbital geometry. Thus, a better mission-design-oriented parameter set would have (μ, ω) as the repeat variables and keep a_0 and r_0 separate. An alternative would be the following modified Π-groups:

$$\Pi_a \equiv \frac{a_0}{\mu^{1/3}\, \omega^{4/3}}, \tag{19a}$$

$$\Pi_r \equiv \frac{r_0\, \omega^{2/3}}{\mu^{1/3}}, \tag{19b}$$

$$\Pi_t \equiv \omega\, t_f. \tag{19c}$$

The two sets are related by an invertible algebraic change of variables:

$$\xi \;=\; \Pi_a\, \Pi_r^2, \qquad \dot{S} \;=\; 2\pi\, \Pi_r^{3/2}, \qquad S \;=\; \Pi_t. \tag{20}$$

In other words, $\{\Pi_a, \Pi_r, \Pi_t\}$ and $\{\xi, \dot{S}, S\}$ are two coordinate systems on the same three-dimensional manifold of initial conditions.

2. Effect of Π_a

The Π_a parameter is related to sail design. When the characteristic acceleration is changed, then Π_a changes with it while all other Π-groups remain fixed. Thus, the effect of Π_a will be analyzed by sweeping through different a_0 values while keeping everything else fixed.

Figure 6 shows performance for a 90° inclination, 45° RAAN, GEO initial altitude transfer as a function of Π_a for different values of transfer duration. The vertical lines mark the Π_a values obtained for Earth parameters for three representative values for a_0: current ($\Pi_a = 0.584$, $a_0 = 0.05$ mm/s^2), near-term ($\Pi_a = 1.169$, $a_0 = 0.1$ mm/s^2), and future ($\Pi_a = 11.688$, $a_0 = 1.0$ mm/s^2) sail technology.

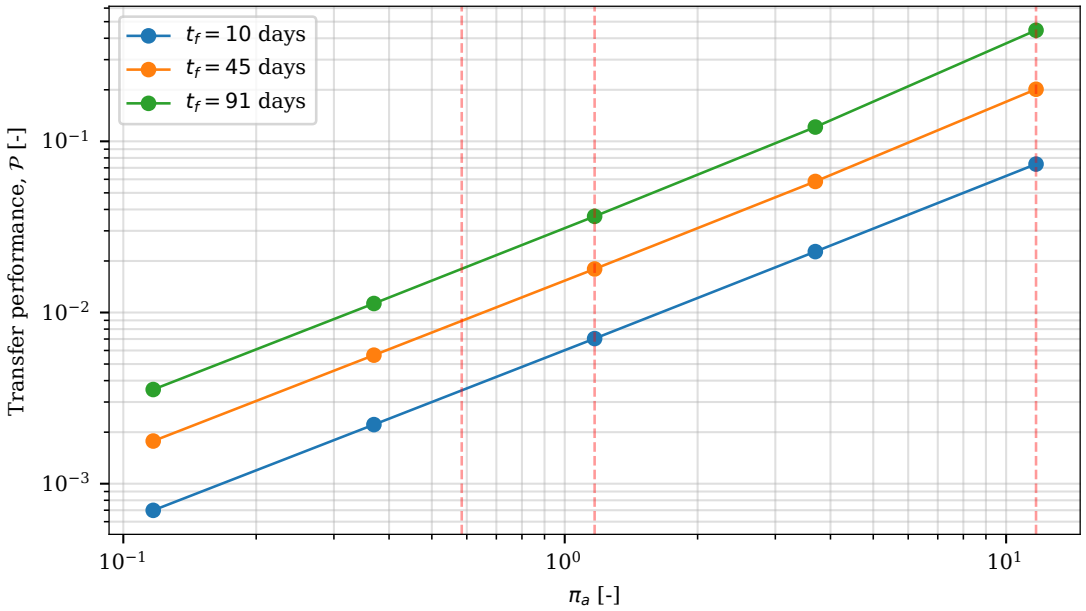

Fig. 6 Transfer performance as a function of Π_a for different transfer durations. Current, near-term, and future sail designs marked with red vertical lines: $i = 90°$, $\Omega = 45°$, $r_0 = 42164$ km

In Figure 6, the transfer performance over the swept range follows a power-law relation with Π_a which can be written as:

$$\mathcal{P} \propto \Pi_a^{p_a}, \tag{21}$$

where p_a is the slope of the power-law relationship. The slope is found to be $p_a = 1.0$ by fitting a power-law curve to the transfers shown in Figure 6. The slope value is then validated to hold also for other values of inclination, RAAN, initial altitude, and durations. The power law allows for a comparison of transfer performance between different sail designs. Given a specific mission scenario (initial radius, transfer duration, orbital geometry, primary), one can optimize the transfer for a benchmark value of characteristic acceleration and use the extrapolation model to efficiently calculate the transfer performance for all other characteristic acceleration values. For example, Figure 6 shows that a 45-day transfer with an ACS3-like characteristic acceleration of $a_0 = 0.05$ mm/s^2 at an inclination of 90° and a RAAN of 45° leads to a roughly 0.9% radius gain, while near-term and future values of a_0 with the same orbital geometry would lead to approximately 1.9% and 20% radius gains, respectively.

3. Effect of Π_r

The Π_r parameter is related to the initial orbital radius of the sail. When the initial radius is changed, then Π_r changes with it while all other Π-groups remain fixed. Thus, the effect of Π_r will be analyzed by sweeping through different r_0 values while keeping everything else fixed.

Figure 7 shows performance for a 90° inclination, 90° RAAN, 0.001 mm/s^2 characteristic acceleration transfer as a function of Π_r for different values of transfer duration. The vertical lines mark the Π_r values obtained for Earth parameters for three representative values for r_0: low Earth orbit (LEO) ($\Pi_r = 0.00324$, $r_0 = 7000$ km at Earth), medium Earth orbit (MEO) ($\Pi_r = 0.00695$, $r_0 = 15000$ km at Earth), and geosynchronous equatorial orbit (GEO) ($\Pi_r = 0.01953$, $r_0 = 42164$ km at Earth) altitudes.

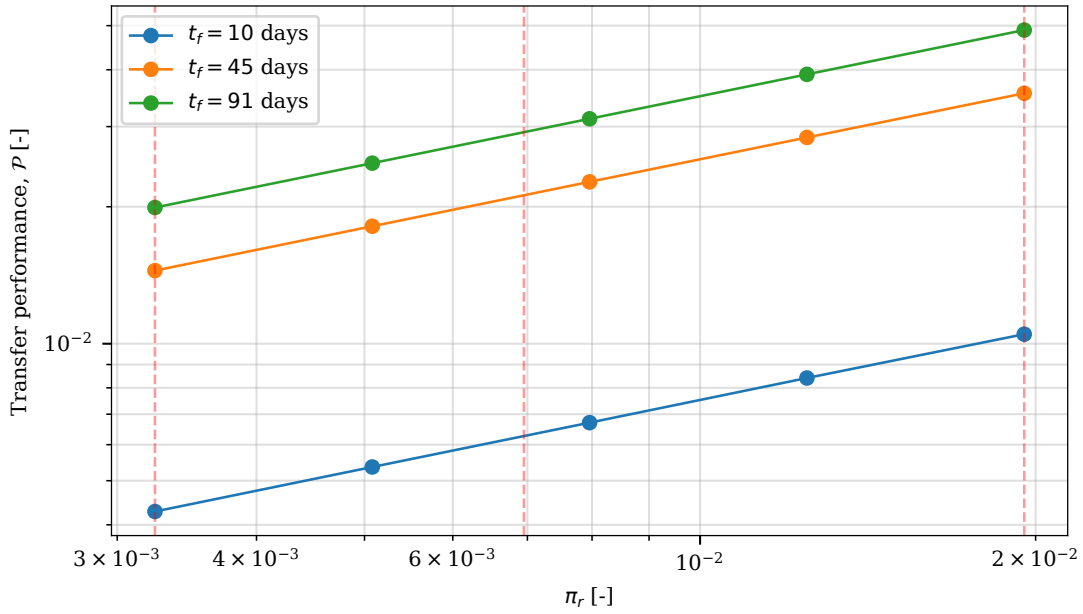

Fig. 7 Transfer performance as a function of Π_r. LEO, MEO, and GEO altitudes marked with red vertical lines: $i = 90°$, $\Omega = 90°$, $a_0 = 0.001$ mm/s^2

Similarly to Π_a, the transfer performance exhibits a power-law relationship with the Π_r group for the swept range which can be written as:

$$\mathcal{P} \propto \Pi_r^{p_r}, \tag{22}$$

where p_r is the slope of the power-law relationship. The slope is found to be $p_r = 0.5$ by fitting a power-law curve to the transfers shown in Figure 7. The slope value is then validated to hold also for other values of inclination, RAAN, characteristic acceleration, and durations. The power law allows for a comparison of transfer performance between different initial radius values. For example, Figure 7 indicates that if a 91-day transfer with 90° inclination, 90° RAAN,

0.001 mm/s^2 characteristic acceleration at LEO altitude would achieve a 2% radius gain, then the same solar sail, with all other parameters fixed, would achieve a 5% radius gain at GEO altitude.

4. Effect of Π_t

The Π_t parameter is related to the duration of the transfer. Different transfer configurations with the same transfer duration (in time) and the same angular velocity of the primary's orbit around the Sun, ω, have the same Π_t value. The same value of Π_t also means that they experience the same solar longitude values over the transfer. The relationship between transfer performance and Π_t is already indirectly shown in Figure 5, where a range of transfer durations is explored while also changing the RAAN to get the best or worst phasing for each transfer duration. Figure 8 shows transfer performance as a function of Π_t for characteristic acceleration of $a_0 = 0.01$ mm/s^2, initial radius of $r_0 = 42164$ km, inclination values of $i = \left[0°,\ 90°\right]$, and RAAN values of $\Omega = \left[0°,\ 90°\right]$.

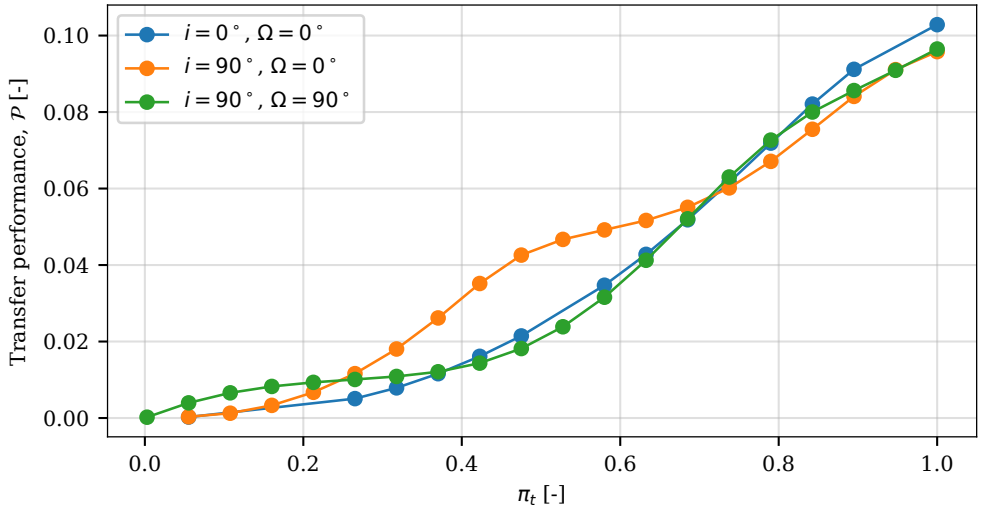

Fig. 8 Transfer performance as a function of Π_t: $a_0 = 0.01$ mm/s^2, $r_0 = 42164$ km

In Figure 8, the resulting radius gain increases with the value of Π_t while exhibiting some periodic oscillations around the mean increase. This trend is tightly connected to the transfer envelopes shown in Figure 5, where the start-phase is modified to match the best or worst possible start-phase for given duration. In Figure 8, each line corresponds to a fixed RAAN (consequently also a fixed start-phase) while the duration is increased. As a result of that, at some transfer durations the fixed start-phase value corresponds to the best possible phasing and at other transfer durations to the worst possible phasing. Thus, the lines in Figure 8 show the expected performance increase with time while oscillating inside the possible transfer envelope for the given inclination.

5. Transfer Performance Extrapolation Model

Both Π_a and Π_r exhibit a power-law relationship with transfer performance. A compact scaling model for the dimensionless performance is:

$$\mathcal{P} \propto \Pi_a^{p_a} \, \Pi_r^{p_r} \quad \text{for fixed } (\Pi_t,\, i,\, \Omega), \tag{23}$$

where the (unspecified) proportionality factor depends on Π_t, i, and Ω but is independent of Π_a and Π_r. To use the model, one needs to first calculate the proportionality factor by optimizing a baseline trajectory, and then the slopes can be used to extrapolate from the baseline transfer performance to the target performance. Substituting the Π-group definitions yields the corresponding dimensional model:

$$\mathcal{P} \propto a_0^{p_a} \, r_0^{p_r}. \tag{24}$$

In previous sections is was shown that the slope values are equal to $p_a = 1.0$ and $p_r = 0.5$. Using these exponents, the transfer performance can be extrapolated through different initial orbital altitudes and different sail designs.

To demonstrate the application of the scaling model shown in Eq. (24), an example extrapolation case is described. The baseline is a transfer at MEO initial altitude ($r_0 = 15000$ km) with sail characteristic acceleration of $a_0 = 0.1$ mm/s^2. Orbital inclination and RAAN are fixed at 90° and 0°, respectively. This baseline transfer is optimized for different durations ranging from one day to 0.2 years. Equation (24) is then used to predict the transfer performance at GEO initial altitude ($r_0 = 42164$ km) with sail characteristic acceleration of 0.05 mm/s^2 while keeping incination and RAAN fixed. For validation, the extrapolated transfers are also optimized to evaluate the extrapolation accuracy. The comparison between extrapolated transfer performance and optimized transfer performance is shown in Figure 9. The extrapolation results are close to the true optimized results. The root-mean-square relative error between the extrapolated and optimized values is computed as 0.37%, indicating a high level of agreement between the two.

IV. Indirect Method Analysis

This section focuses on the method used to optimize the transfers that are analyzed in Section III. First, the sensitivity of the solution vector, $\boldsymbol{w}$, with reference to the problem parameters is analyzed to show the effectiveness of continuation methods. Secondly, the convergence of the indirect method is analyzed for different solvers and problem setups.

A. Sensitivity of the Indirect Method

The sensitivity of the indirect method describes how sensitive the solution elements are to changes in the parameters of the problem a_0, r_0, θ_f, i, and Ω. It is useful if the solution elements change smoothly with the input parameters because this allows for continuation methods and homotopy to solve more difficult transfer configurations that would

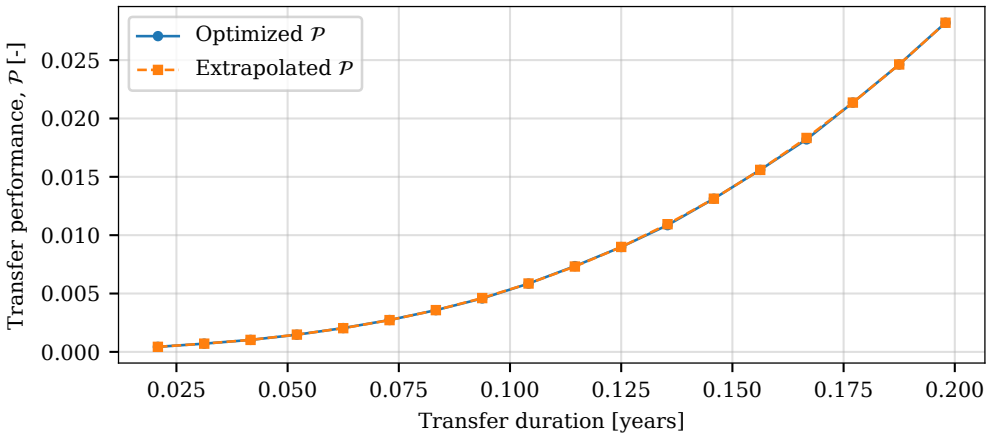

Fig. 9 Extrapolation results from MEO a_0 = 0.1 mm/s^2 to GEO a_0 = 0.05 mm/s^2

otherwise not converge from a trivial initial guess.

To visualize the progression of the solution components with changes in input parameters, a benchmark 10-revolution transfer around Earth is taken. The initial radius is set to r_0 = 42164 km, the characteristic acceleration to a_0 = 0.05 mm/s^2, the inclination to i = 45°, and the RAAN to Ω = 90°. Each parameter is then swept across a range while everything else is kept constant to analyze the effect of individual parameter changes on the solution. The initial radius is swept from LEO (7000 km) to GEO (42164 km), the characteristic acceleration is swept from a_0 = 0.001 mm/s^2 to a_0 = 1.0 mm/s^2, the transfer duration is swept from one-revolution to 82-revolutions, and the inclination and RAAN are swept within their valid bounds. The results of this process are shown in Figure 10.

As shown in Figure 10, the solution elements change smoothly with all problem input parameters. This is a good sign that continuation methods can be used to solve more challenging transfer configurations. For example, the solution from a 90° inclination transfer, which has the best illumination conditions [22], can be used as an initial guess for a lower inclination transfer. This process can be repeated in small inclination increments until reaching a 0° transfer, which is more challenging than the 90° transfer due to less favorable illumination conditions. This continuation method was used to produce many of the results seen in Section III.

Furthermore, Figure 10 reveals that the Lagrange multipliers (ν_1 and ν_2) closely follow the velocity costates ($\lambda_{\bar{u}}$ and $\lambda_{\bar{v}}$). The cause of that can be inferred from Figure 11 where the evolution of costates with the argument of latitude is given for the benchmark transfer. It is evident that the costates are periodic with the orbital period of the sail. In the angle formulation, one can specify the transfer duration as an integer number of revolutions, which forces the transfer to begin and end at the same angular position. Due to the periodicity, it is expected that the primer vector (defined by $\lambda_{\bar{u}}$ and $\lambda_{\bar{v}}$) at the initial state points in the same direction as the primer vector at the final state (defined by $\lambda_{\bar{u}}$ and $\lambda_{\bar{v}}$ at θ_f or ν_1 and ν_2). The costate related to the radius $\lambda_{\bar{r}}$ shows the same trends as $\lambda_{\bar{v}}$ and ν_2. Equation (10) indicates that ν_2

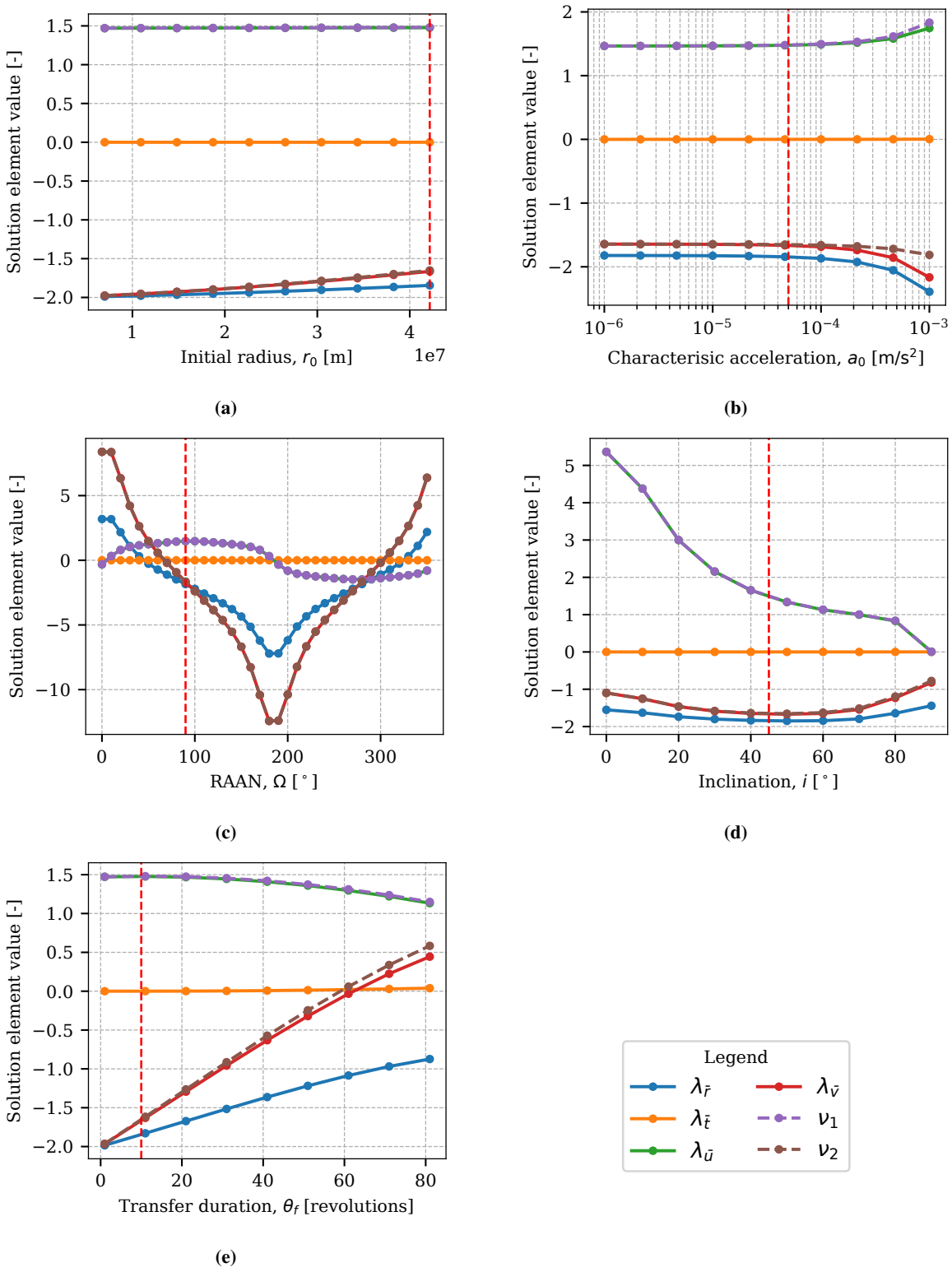

Fig. 10 Sensitivity of the solution elements with reference to the problem input parameters: a) Initial radius, b) Characteristic acceleration, c) RAAN, d) Inclination, and e) Transfer duration. Benchmark transfer parameters marked with red vertical lines.

also contributes to the terminal boundary condition of $\lambda_{\bar{r}}$, which is the reason for the similar trend. Finally, the costate related to scaled time, $\lambda_{\bar{t}}$, stays relatively close to 0 at all times. These findings help to constrain the initial guess and reduce the search space when a hard-to-converge problem needs to be solved.

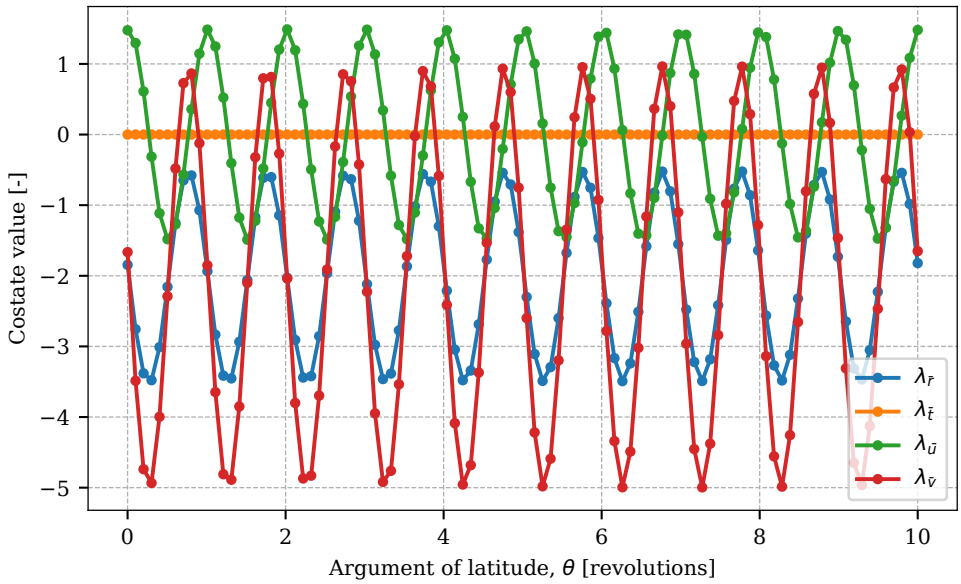

Fig. 11 Evolution of the costates with transfer duration for the benchmark 10-revolution transfer.

B. Convergence of the Indirect Method

A major difficulty in using indirect techniques is that the solution is very sensitive to the initial costate values [24]. This subsection aims to quantify that sensitivity and calculate convergence basins for different solvers and problem configurations. First, Section IV.B.1 examines the differences in convergence between two different solvers: one using finite-differences for root-finding and the other using automatic differentiation. Secondly, Section IV.B.2 describes how the problem configuration (e.g., orbit geometry, transfer duration, sail characteristic acceleration) affects convergence. Finally, Section IV.B.3 examines the effect of specific costate-pairs on convergence.

The convergence of the indirect shooting method is studied as a function of the distance and the direction of the initial costate guess from a reference solution. For a benchmark transfer problem, the reference solution $\boldsymbol{w}^\star = [\lambda_{\bar{r}}, \lambda_{\bar{t}}, \lambda_{\bar{u}}, \lambda_{\bar{v}}, \nu_1, \nu_2]$ is computed by solving the shooting problem from a trivial initial guess or using numerical continuation. Then, the reference solution is perturbed proportionally to its magnitude:

$$\boldsymbol{w} = \boldsymbol{w}^\star + \left\|\boldsymbol{w}^\star\right\| \cdot l \cdot \boldsymbol{\eta}, \tag{25}$$

where l is the perturbation magnitude and η is the direction of the perturbation sampled from a six-dimensional unit

sphere. A range of perturbation magnitudes is swept and, at each magnitude value, a number of directions is sampled. The convergence statistics are then captured and aggregated over the perturbation magnitude. By aggregating the results for different perturbation directions, no insight is gained into the effect of the initial guess of specific costate values (direction of the perturbation), but a sufficient sample size and unbiased sampling through the unit sphere guarantees a fair overview of the convergence basin. For full reproducibility of the convergence basins, the NumPy random number generator was seeded with seed = 123 before each analysis. The resulting metric is the success rate per perturbation magnitude bin which is the ratio of runs that converged to the total number of runs in the bin. The convergence basin is then plotted as the success rate as a function of the perturbation magnitude. This process of calculating the convergence basin is henceforth called the convergence analysis with the range of perturbation magnitudes and the number of directions specified at the start of each analysis separately.

1. Influence of the differentiation method on the convergence of the algorithm

During the process of this work, two root-finders were used to solve the TPBVP. First, the *scipy.fsolve* function was used, which is a general-purpose numerical root-finding function from the SciPy Python library that uses MINPACK's hybrid Powell method [32]. In parallel, the *jaxopt.ScipyRootFinding* function was used from the JAXopt Python library. JAXopt integrates the same SciPy solvers with JAX's automatic differentiation system, allowing gradients to be computed through the root-finding process [33]. In the following paragraphs, the convergence characteristics of the two methods are compared.

The benchmark problem chosen for this analysis is a one-revolution transfer at Earth with a characteristic acceleration value of $a_0 = 0.05$ mm/s^2, an initial radius value of $r_0 = 42164$ km, an inclination of $i = 90°$, and a RAAN of $\Omega = 90°$. The convergence analysis is performed using both the *scipy.fsolve* function and the *jaxopt.ScipyRootFinding* function with perturbation magnitudes ranging from 10^{-3} to 10^6 and 100 directions sampled at each perturbation magnitude. The results are shown in Figure 12. The solid lines show the success rate while the dashed lines show the number of function evaluations. The JAXopt statistics are given in orange and the SciPy statistics are given in blue.

Figure 12 shows that the convergence characteristics are better for the *jaxopt.ScipyRootFinding* function compared to the *scipy.fsolve* function. The success rate for the JAXopt formulation is higher through larger perturbation magnitudes, and convergence also requires far fewer function evaluations. This result is expected because JAXopt is able to use the automatic differentiation from the JAX framework to provide the exact Jacobian of the shooting function to the solver. On the other hand, the SciPy's *fsolve* function has to rely on finite-difference Jacobians of the shooting function, which are less accurate than the exact Jacobians provided by automatic differentiation. An exact Jacobian evaluation allows the solver to converge more easily and with fewer function evaluations. A similar trend can be observed by sampling perturbation magnitudes from 10^{-3} to 10^4 and plotting each optimization attempt as an individual scatter point, rather than aggregating results over perturbation-magnitude bins as done previously. The outcome of this analysis is shown in

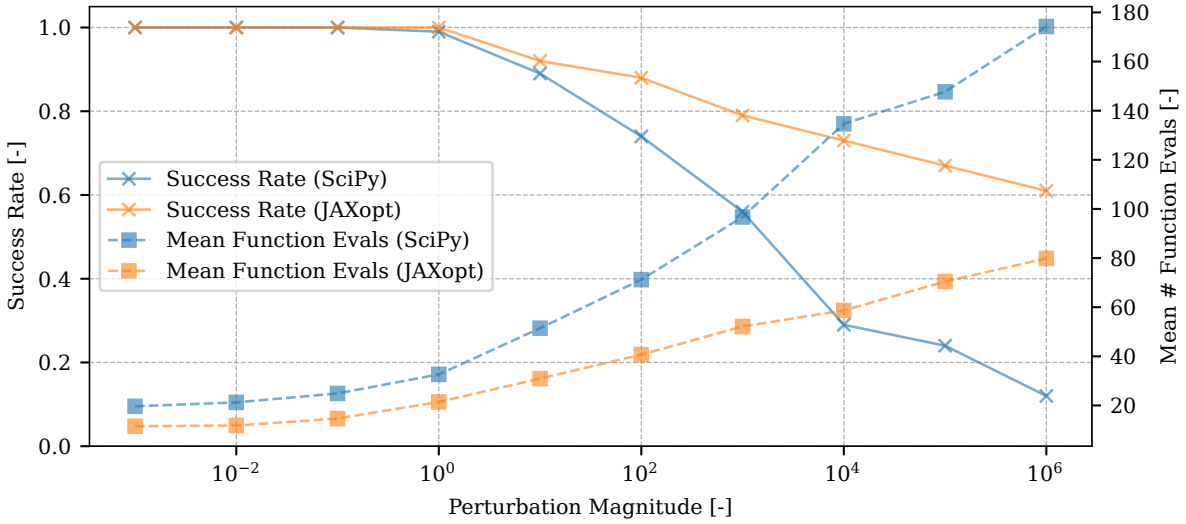

Fig. 12 Convergence comparison between *scipy.fsolve* and *jaxopt.ScipyRootFinding* for a one-revolution benchmark transfer.

Figure 13a. Each data point on the plot represents a single optimization attempt, with successful cases marked by circles and unsuccessful ones marked by crosses.

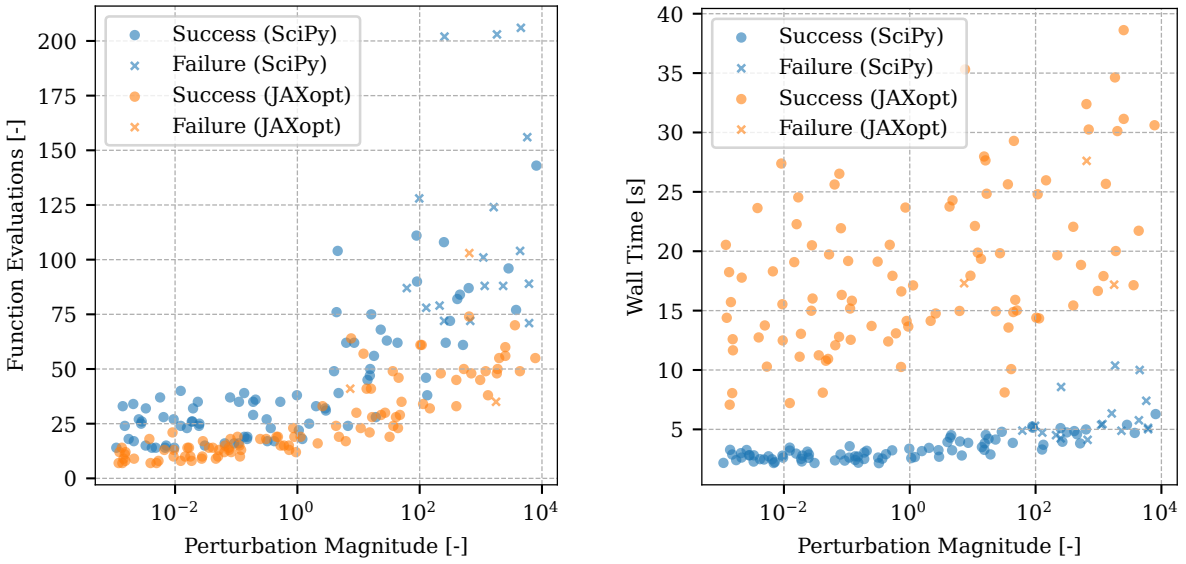

(a) **(b)**

Fig. 13 Comparison of convergence and execution time for sampled perturbation magnitudes in the one-revolution benchmark transfer: a) Number of function evaluations and b) Wall clock time

Inspection of Figure 13 reveals that the variation in the number of function evaluations is larger for the SciPy solver compared to the JAXopt solver. That variation grows for both methods with the perturbation magnitude. The increased

convergence from JAXopt comes at a cost of increased computational time, however. The wall-clock times of the optimizations presented in Figure 13a are shown in Figure 13b. It is apparent that the JAXopt optimizations take much more time compared to the SciPy optimizations. That is because the forward-mode automatic differentiation used by JAXopt pushes derivative information through every operation, so each evaluation requires more work than a traditional function call. So even with the reduced number of "shots" needed due to the exact Jacobian, the whole optimization still takes more time due to the calculation of the exact Jacobian.

In general, both solvers perform well in terms of convergence. The success rate only begins to decrease once the perturbation magnitude becomes comparable to the length of the benchmark solution vector, and both solvers maintain a high success rate until the perturbations reach values several orders of magnitude larger than the benchmark solution. The theoretically worse SciPy solver only sees a significant increase in function evaluations and decrease in success rate at a perturbation magnitude value of 10^1 which corresponds to a perturbation magnitude 10 times larger than the solution vector itself. The question of which method to use is still a trade-off between wall-clock time and convergence. If a specific transfer configuration needs to be optimized, then JAXopt will converge more reliably, while if a range of transfer configurations needs to be optimized, then SciPy should be used due to the reduction in processing time. In the following sections, *scipy.fsolve* is used for that exact reason.

2. Problem configuration effect on convergence

This subsection focuses on the effect of the problem parameters on convergence. The convergence analysis is performed for all possible combinations of the problem parameters given in Table 1. For each problem configuration, the benchmark solution was perturbed at 10 different perturbation magnitudes from 10^{-5} to 10^4. At each perturbation magnitude, 20 different perturbations were sampled. The durations of 91 and 182 revolutions were selected because, at GEO altitude, they correspond most closely to quarter-year and half-year intervals, respectively, even though transfers to higher orbits result in actual times slightly exceeding these fractions of a year.

Table 1 Swept parameters and fixed parameters in the convergence study.

Swept parameters	
Duration, θ_f	$\{1, 45, 91, 182\}$ revolutions
Right ascension of ascending node, Ω	$\{0, 90\}^\circ$
Inclination, i	$\{0, 90\}^\circ$
Characteristic acceleration, a_0	$\{0.05, 0.1\}$ mm/s^2
Initial radius, r_0	$\{21{,}371{,}000, 42{,}157{,}000\}$ m
Fixed parameters	
Primary	Earth
Gravitational parameter, μ	$3.986004418e14$ m^3/s^2
Primary mean motion around the Sun, ω	1.14075×10^{-5} $^\circ$/s

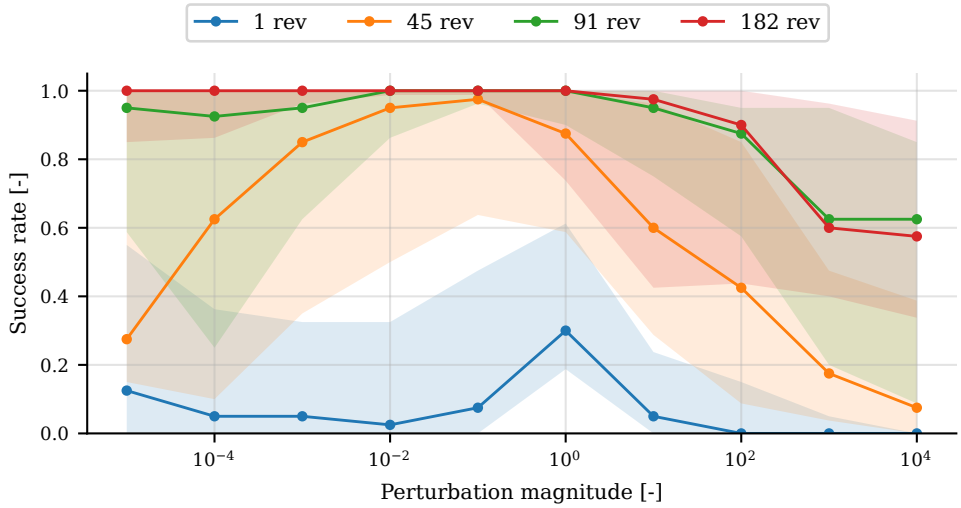

Fig. 14 Aggregated convergence basins for transfer duration values of $\theta_f = \left[1,\ 45,\ 91,\ 182\right]$ revolutions.

The effect of transfer duration on convergence is shown in Figure 14. For each unique transfer duration in Table 1, the success rates of all combinations with that transfer duration are aggregated. The solid line then shows the median of the success rates of the convergence basins with this duration and the shaded region shows the interquartile range (IQR). First, it is evident that short transfers have the lowest success rates and consequently the smallest convergence basins. With little time, the sail has limited authority to satisfy both circularity constraints at the endpoint and grow the radius, and the residual function $\boldsymbol{F}(\boldsymbol{w})$ becomes stiff and anisotropic. Figure 14 shows a trend where the convergence basins grow with transfer duration. The convergence is significantly better at 91- and 182-revolution transfers compared to 1- and 45-revolution transfers. This result is somewhat unintuitive because the expectation is that the sensitivity of the final state to the initial guess would increase with duration, also affecting convergence, but this is not the case.

To assess the sensitivity of the residual function $\boldsymbol{F}(\boldsymbol{w})$, the condition number of the Jacobian, $\mathcal{W}$, can be plotted. The condition number is defined as:

$$\kappa(\mathcal{W}) = \frac{\sigma_{max}(\mathcal{W})}{\sigma_{min}(\mathcal{W})}, \tag{26}$$

where $\sigma_{max}(\mathcal{W})$ and $\sigma_{min}(\mathcal{W})$ are the maximal and minimal singular values of the Jacobian [37]. Smaller values for κ indicate better conditioning. Figure 15 shows κ versus transfer duration for a GEO initial altitude, 0.05 mm/s^2 characteristic acceleration, 0° inclination, and 0° RAAN transfer for different transfer durations. The condition number is evaluated at a nominal constant initial guess of $\boldsymbol{w} = \left[1.0, 1.0, 1.0, 1.0, 1.0, 1.0\right]$. The vector of ones is used because it is sufficiently far from the true solution and serves as a natural nominal guess in cases where no informed initialization is available. In accordance with the results shown in Figure 14, the residual function is most ill-conditioned at very

short durations, after which the condition number steadily decreases as the duration increases. This means that at short durations the residual function is highly sensitive to the initial guess, making convergence difficult.

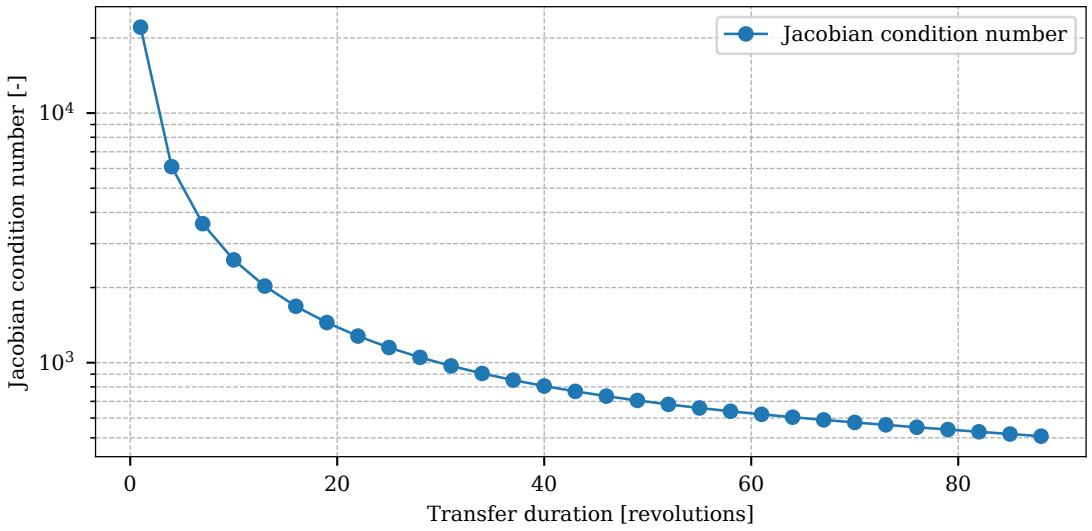

Fig. 15 Condition number of the Jacobian at a nominal constant initial guess of $w = \left[1.0, 1.0, 1.0, 1.0, 1.0, 1.0\right]$ as a function of the transfer duration. $i = 0°$, $\Omega = 0°$, $r_0 = 42164$ km, $a_0 = 0.05$ mm/s^2

The convergence for different inclination values is shown in Figure 16a. It is clear that an inclination value of $i = 0°$ is generally harder to converge for compared to an inclination value of $i = 90°$. The sail acts in-plane through the projection of the ideal 3D sail-acceleration bubble onto the orbital plane, and the shape and time variation of that projection depend on the orientation of the Sun-line with reference to the orbital plane [22]. At an inclination of $i = 0°$, the Sun-line lies in the plane at all times. The admissible set of controls becomes highly directional (aligned with the Sun-line), leading to a more complex control law, which is numerically adverse to the solver. At an inclination of $i = 90°$, the angle between the orbital plane and the Sun-line is larger, leading to a more isotropic set of controls over an orbit. As a result, the control law is smoother with reference to the initial guess and the Jacobian is better conditioned.

The convergence behavior for different initial radius values is shown in Figure 16b. Higher initial radius configurations exhibit better convergence compared to the lower initial radius ones. At present, there is no clear explanation for this behaviour. A possible reason is that, at higher altitude for the same number of revolutions, there is more time for the sail to act over the trajectory. Additionally, with the increase of initial radius, the magnitude of the gravitational acceleration decreases and subsequently, the influence of the sail over the trajectory increases. Intuitively, a larger control authority could lead to better convergence due to enhanced controllability.

Many convergence basins exhibit a trend where convergence is bad near the solution, then gets better at the middle of the perturbation range, and then decreases again as perturbation magnitude grows large; an inverted-U pattern. Two 45-revolution transfer configurations can be extracted to explain this: one with the inverted-U pattern ($r_0 = 42157$ km,

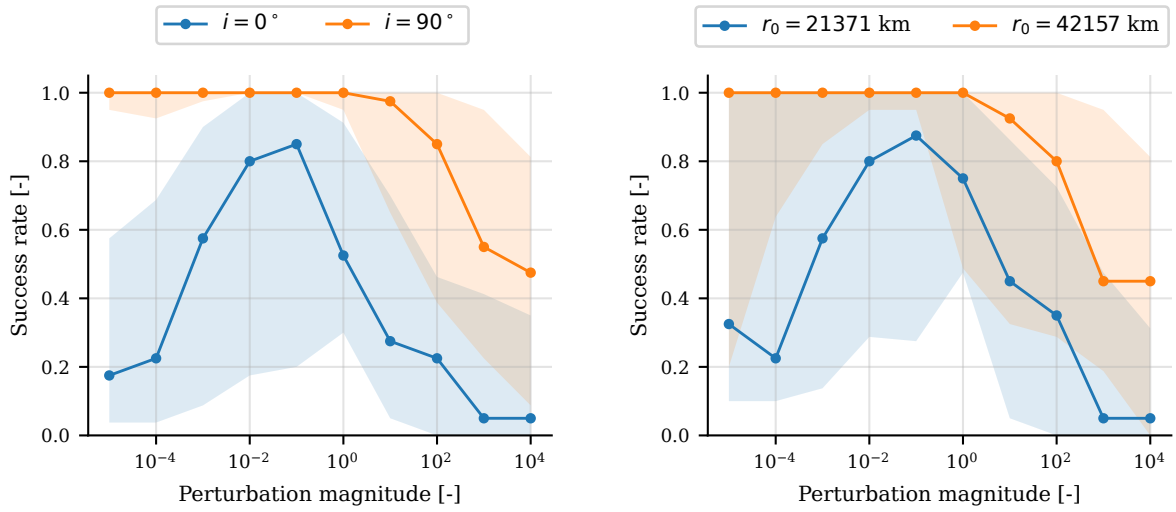

(a) **(b)**

Fig. 16 Aggregated convergence basins for a) inclination values of $i = \left[0,\ 90\right]$ degrees and b) initial radius values of $r_0 = \left[21371,\ 42157\right]$ km.

$a_0 = 0.05$ mm/s^2, $i = 0°$, $\Omega = 0°$) and one without ($r_0 = 42157$ km, $a_0 = 0.05$ mm/s^2, $i = 90°$, $\Omega = 90°$). The condition number of the Jacobian can then be plotted as a function of the perturbation magnitude, as shown in Figure 17. A similar process to the convergence analysis is performed by sampling perturbation magnitudes from 10^{-3} to 10^3, with 12 perturbations per magnitude bin. However, instead of attempting to solve the problem from each initial guess, only the Jacobian condition number is computed and the results are aggregated within each magnitude bin. The solid curves represent the median condition number at each magnitude, while the shaded regions indicate the interquartile range.

Analysis of Figure 17 indicates that the problem associated with the regular convergence trend (blue line) has a low Jacobian condition number at the solution (well-posed problem, good convergence), and then, with increasing perturbation magnitude, the condition number also grows, indicating higher sensitivity and lower convergence. Conversely, the inverted-U pattern problem (orange line) already has an elevated condition number at the benchmark value, indicating high sensitivity near the solution. Then, as the perturbation magnitude increases, the condition number initially decreases, so the problem becomes better posed. This is the reason for the peak in the pattern where convergence increases. After the dip, the condition number starts increasing together with perturbation magnitude, as is the expected trend.

3. Pairwise directional convergence

The solution vector can be divided into pairs, where $\{\nu_1,\ \nu_2\}$ are the Lagrange multipliers, $\{-\lambda_{\bar{u}},\ -\lambda_{\bar{v}}\}$ the initial primer vector direction, and $\{\lambda_{\bar{r}},\ \lambda_{\bar{t}}\}$ the remaining pair. In this section, the effect of these distinct pairs on convergence

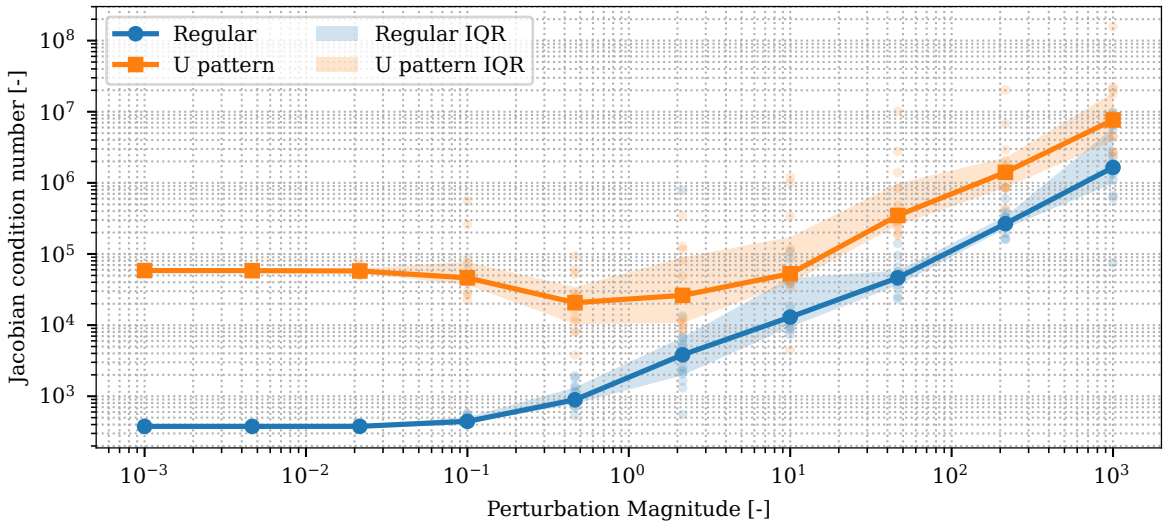

Fig. 17 Condition number of the Jacobian versus perturbation magnitude for a regular convergence basin and a convergence basin with an inverted-U pattern. $r_0 = 42157$ km, $a_0 = 0.05$ mm/s^2, regular: $i = 0°$, $\Omega = 0°$, U-pattern: $i = 90°$, $\Omega = 90°$.

is studied.

This analysis is performed on a benchmark two-revolution transfer at GEO altitude, 45° inclination, 0° RAAN, and a sail characteristic acceleration of $a_0 = 0.1$ mm/s^2. For each pair $(w_i,\ w_j)$, the benchmark solution $(w_i^\star,\ w_j^\star)$ is first expressed in polar form:

$$\rho_{ij} = \left\|[w_i^\star,\ w_j^\star]\right\|, \qquad \beta_{ij} = \tan^{-1}\left(w_j^\star,\ w_i^\star\right).$$

A two-dimensional polar grid is then constructed by sampling 10 radii uniformly between $0.1 \cdot \rho_{ij}$ and $2.0 \cdot \rho_{ij}$ and 20 angles uniformly across a full 360° interval. For all samples on the grid, only this pair of components is perturbed and the remaining four costate components are kept fixed at their benchmark values. For each point on the grid, the modified vector is supplied as an initial guess to the shooting method. The resulting convergence plots are shown in Figure 18 where green points indicate successfully converged initial guesses and red dots indicate initial guesses that did not converge. The benchmark solution is marked with a star.

Multiple trends emerge from Figure 18. First, as seen in Figure 18b, the convergence is highly dependent on the direction of the primer vector $\{-\lambda_{\bar{u}},\ -\lambda_{\bar{v}}\}$. The problems converge more consistently when the direction of the primer vector in the initial guess is close to that of the benchmark primer vector. This implies that, if the direction of the primer vector at the initial epoch could be estimated reliably, even with a poor guess for its magnitude, substantially more robust initial guesses could be constructed. Secondly, the Lagrange multipliers $\{\nu_1,\ \nu_2\}$ swept in Figure 18c have almost no visible influence on convergence. This is expected: the Lagrange multipliers do not affect the forward

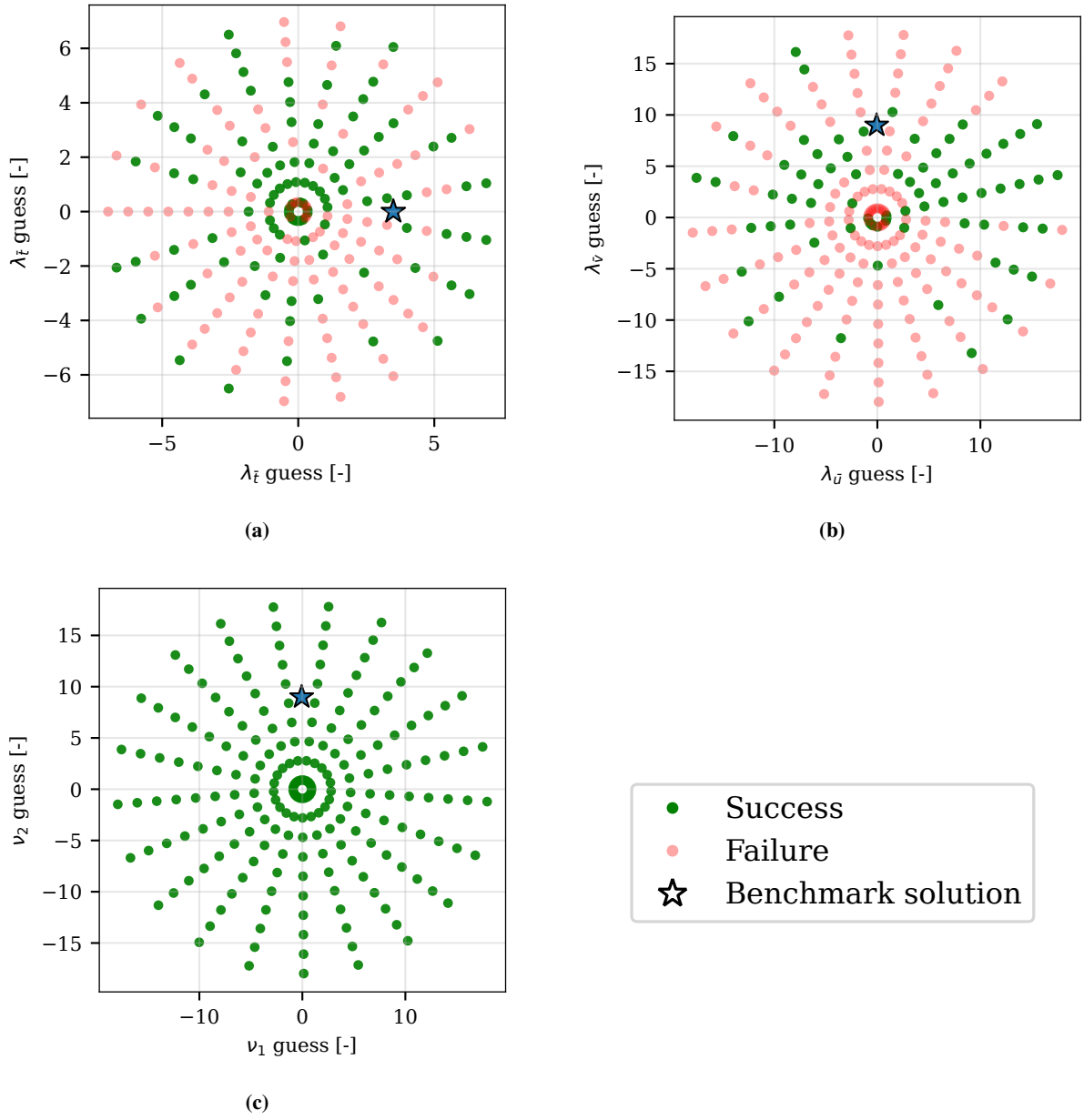

Fig. 18 Directional convergence analysis. Sweeping a) $\{\lambda_{\bar{r}},\ \lambda_{\bar{t}}\}$, b) $\{\lambda_{\bar{u}},\ \lambda_{\bar{v}}\}$, and c) $\{\nu_1,\ \nu_2\}$. $\theta_f = 2$ revs, $i = 45°$, $\Omega = 0°$, $r_0 = 42164$ km, $a_0 = 0.1$ mm/s^2

propagation and only enter through the terminal residual. Since the remaining solution components are fixed at their benchmark values, the forward integration already follows the optimal trajectory and the solver only needs to adjust the multipliers to satisfy the constraints. A coupled perturbation of the Lagrange multipliers together with some of the costates might still impact convergence, but this case is not explored here. Finally, when sweeping the pair $\{\lambda_{\bar{r}},\ \lambda_{\bar{t}}\}$, no sharp directional pattern is observed within the explored range. Successful and unsuccessful guesses are interspersed and convergence does not appear to be controlled by a single dominant direction or by the magnitude of this pair alone.

Taken together, the results in Figure 18 suggest a broader qualitative picture. Convergence of the indirect method is most sensitive to the orientation of those costate components that directly determine the control law (here, the primer vector), while it is comparatively insensitive to their absolute magnitude and to components that only appear in the terminal constraints (the Lagrange multipliers). When the initial costate direction is roughly aligned with the true optimal direction, the solver can tolerate relatively large magnitude errors and still converge efficiently. This indicates that reliable estimation of costate directions, whether via analytical approximations, continuation from nearby problems, or simpler orbit-raising solutions, can substantially increase the likelihood of convergence, even when the corresponding magnitudes are only coarsely approximated.

V. Conclusions

This study developed and applied an indirect optimization framework to characterize planar, planetocentric solar sail circular-to-circular (C2C) transfers. By formulating the problem using the Calculus of Variations and Pontryagin's Maximum Principle, the optimal control problem (OCP) was reduced to a finite-dimensional Two-Point Boundary Value Problem (TPBVP). This TPBVP was solved using a single-shooting method enhanced with JAX-based automatic differentiation, which proved more robust than standard finite-difference approaches. Applying this framework yielded several key insights into both the mission physics and the numerical method.

It was demonstrated that the transfer performance (i.e., radius change over initial radius, $\mathcal{P} = \Delta r/r_0$) is highly dependent on the start-phase, γ_0, which defines the start time of the transfer relative to the orbit of the primary around the Sun, or in other words, the orientation of the orbital plane with reference to the Sun-line at the initial time step. This study rigorously validates the phasing heuristics established in recent patched-method literature. Specifically, the indirect optimization results confirm that, for a given transfer duration, there exist two γ_0 values that lead to the best transfer performance and two γ_0 values that lead to the worst transfer performance. The performance is best when the Sun-line becomes perpendicular to the line of nodes at the midpoint of the transfer, while performance is worst when the Sun-line becomes parallel to the line of nodes at the midpoint. This effect is dominant for high-inclination orbits with respect to the ecliptic ($i = 90°$) and negligible for low-inclination orbits ($i = 0°$) due to the latter having constant illumination conditions at all times. Additionally, it was found that, when the duration of the transfer is less than a year, the best-phased $i = 90°$ cases have the largest radius gain. For transfer times near a year, lower-inclination transfers outperform the $i = 90°$ case.

Dimensional analysis was used to reduce the five-dimensional input space of the problem into three independent Π-groups: Π_a, Π_r, and Π_t. Each group contains only one of the primary mission design variables (acceleration, radius, or time), enabling isolated variation of each variable. Numerical analysis revealed a simple power-law relationship for transfer performance: $\mathcal{P} \propto \Pi_a^{1.0}\Pi_r^{0.5}$. This model was shown to accurately extrapolate performance across different sail designs (a_0) and initial altitudes (r_0) from a single benchmark optimization, providing an effective tool for first-order

trade-off studies.

The indirect method was analysed in terms of both sensitivity and convergence. It was shown that, in general, the solution elements (the initial values of the four costates and the two constant Lagrange multipliers) vary smoothly with the transfer parameters. This behaviour indicates that continuation methods can be used effectively to reach convergence for difficult transfer configurations that would otherwise not converge from a trivial initial guess. The convergence analysis further revealed that increasing the transfer duration improves convergence, owing to better conditioning of the residual-function Jacobian. In addition, low-inclination transfers exhibit smaller convergence basins due to poor illumination conditions, and lower initial-radius values perform worse than higher initial-radius values. Finally, it was shown that the direction of the primer vector in the initial guess is more important for convergence than its magnitude.

It is important to note the limitations of this study, which also define avenues for future work. The analysis was constrained to planar transfers and employed a simplified dynamical model using an ideal solar sail and accounting only for point-mass gravity. Real-world missions would be subject to significant 3D effects and perturbations, including non-ideal sail optical properties, third-body gravity, aerodynamic drag, and periodic eclipses, all of which were neglected here. Furthermore, the heliocentric motion of the primary is assumed circular, and no control constraints were enforced. Future work should extend the framework to out-of-plane dynamics and non-ideal sails and incorporate eclipses and higher-order perturbations (e.g., J_2 and third-body effects).

Appendix

References

[1] McInnes, C. R., "Solar Sailing: Technology, Dynamics and Mission Applications," 1999.

[2] Sawada, H., Mori, O., Okuizumi, N., Shirasawa, Y., Miyazaki, Y., Natori, M., Matunaga, S., Furuya, H., and Sakamoto, H., "Mission Report on The Solar Power Sail Deployment Demonstration of IKAROS," 2011. https://doi.org/10.2514/6.2011-1887.

[3] Spencer, D. A., Betts, B., Bellardo, J., Diaz, A., Plante, B., and Mansell, J. R., "The LightSail 2 solar sailing technology demonstration," *Advances in Space Research*, 2021. https://doi.org/10.1016/j.asr.2020.06.029.

[4] Wilkie, W. K., *Overview of the NASA Advanced Composite Solar Sail System (ACS3) Technology Demonstration Project*, AIAA Scitech Forum, 2021, Chap. 1, p. 2. https://doi.org/10.2514/6.2021-1260, URL https://arc.aiaa.org/doi/abs/10.2514/6.2021-1260.

[5] Otten, M., and McInnes, C., "Near Minimum-Time Trajectories for Solar Sails," 2001. https://doi.org/10.2514/2.4758.

[6] Dachwald, B., Mengali, G., Quarta, A., and Macdonald, M., "Parametric model and optimal control of solar sails with optical degradation," 2006. https://doi.org/10.2514/1.20313.

[7] Mengali, G., and Quarta, A. A., "Solar sail trajectories with piecewise-constant steering laws," *Aerospace Science and Technology*, 2009. https://doi.org/10.1016/j.ast.2009.06.007.

[8] Quarta, A. A., Mengali, G., and Bassetto, M., "Optimal solar sail transfers to circular Earth-synchronous displaced orbits," *Astrodynamics*, 2020. https://doi.org/10.1007/s42064-019-0057-x.

[9] Carzana, L., Visser, P. N. A. M., and Heiligers, M. J., "Locally optimal control laws for Earth-bound solar sailing with atmospheric drag," *Aerospace Science and Technology*, 2022. https://doi.org/10.1016/j.ast.2022.107666.

[10] Oguri, K., Lantoine, G., Petropoulos, A. E., and McMahon, J. W., "Solar Sailing Q-Law for Planetocentric, Many-Revolution Sail Orbit Transfers," *Journal of Guidance Control and Dynamics*, 2023. https://doi.org/10.2514/1.g007103.

[11] Macdonald, M., and McInnes, C., "Analytical Control Laws for Planet-Centered Solar Sailing," 2005. https://doi.org/10.2514/1.11400.

[12] Macdonald, M., and McInnes, C., "Realistic Earth escape strategies for solar sailing," 2005. https://doi.org/10.2514/1.5165.

[13] Mengali, G., and Quarta, A., "Near-Optimal Solar-Sail Orbit-Raising from Low Earth Orbit," 2005. https://doi.org/10.2514/1.14184.

[14] Sackett, L. L., "Optimal solar sail planetocentric trajectories," *NASA STI/Recon Technical Report N*, 1977.

[15] Kelly, P., and Bevilacqua, R., "Geostationary debris mitigation using minimum time solar sail trajectories with eclipse constraints," *Optimal control applications & methods*, 2020. https://doi.org/10.1002/oca.2676.

[16] Fitzgerald, R., "Characterizing Minimum-Time Solar Sail Geostationary Orbit Transfers Using Pseudospectral Optimal Control," *Journal of Spacecraft and Rockets*, 2021. https://doi.org/10.2514/1.a34950.

[17] Stolbunov, V., Ceriotti, M., Colombo, C., and McInnes, C., "Optimal Law for Inclination Change in an Atmosphere Through Solar Sailing," 2013. https://doi.org/10.2514/1.59931.

[18] Bianchi, C., Niccolai, L., Mengali, G., and Ceriotti, M., "Preliminary design of a space debris removal mission in LEO using a solar sail," *Advances in Space Research*, 2024. https://doi.org/10.1016/j.asr.2024.01.024.

[19] Kelly, P., and Bevilacqua, R., "An optimized analytical solution for geostationary debris removal using solar sails," *Acta Astronautica*, 2019. https://doi.org/10.1016/j.actaastro.2019.05.055.

[20] Barles, A., Ceriotti, M., Ciampa, F., and Felicetti, L., "An optimal steering law for sailing with solar and planetary radiation pressure," *Aerospace Science and Technology*, 2021. https://doi.org/10.1016/j.ast.2021.107051.

[21] Leemans, G., Carzana, L., and Heiligers, M. J., "Many-Revolution Earth-Centred Solar-Sail Trajectory Optimisation Using Differential Dynamic Programming," *AIAA SCITECH 2022 Forum*, 2022. https://doi.org/10.2514/6.2022-1776.

[22] Gámez Losada, F., Visser, P., and Heiligers, M., "Fundamentals of Solar-Sail Transfers Around Planetary Bodies," *Proceedings of the 29th International Symposium on Space Flight Dynamics*, 2024.

[23] Minnozzi, R., "Differential Dynamic Programming for the optimization of many-revolution solar-sail transfers," Master's thesis, TU Delft, 2025.

[24] Morante, D., Rivo, M. S., and Soler, M., "A Survey on Low-Thrust Trajectory Optimization Approaches," *Aerospace*, 2021. https://doi.org/10.3390/aerospace8030088.

[25] Weinert, H., "Bryson, A. E./ Ho, Y.-C., Applied Optimal Control, Optimization, Estimation, and Control. New York-London-Sydney-Toronto. John Wiley & Sons. 1975. 481 S., £10.90," *ZAMM - Journal of Applied Mathematics and Mechanics / Zeitschrift für Angewandte Mathematik und Mechanik*, Vol. 59, No. 8, 1979, pp. 402–402. https://doi.org/https://doi.org/10.1002/zamm.19790590826, URL https://onlinelibrary.wiley.com/doi/abs/10.1002/zamm.19790590826.

[26] Longuski, J. M., Guzmán, J. J., and Prussing, J. E., "Optimal Control with Aerospace Applications," *Springer eBooks*, 2014. https://doi.org/10.1007/978-1-4614-8945-0.

[27] Mengali, G., and Quarta, A., "Optimal Three-Dimensional Interplanetary Rendezvous Using Nonideal Solar Sail," *Journal of Guidance, Control, and Dynamics*, 2005. https://doi.org/10.2514/1.8325.

[28] Carzana, L., Visser, P., and Heiligers, J., "Delft University of Technology Solar-sail control laws for perturbed Earth-bound trajectories," 2021.

[29] Sundman, K. F., "Mémoire sur le problème des trois corps," *Acta Mathematica*, Vol. 36, No. none, 1913, pp. 105 – 179. https://doi.org/10.1007/BF02422379, URL https://doi.org/10.1007/BF02422379.

[30] Bradbury, J., Frostig, R., Hawkins, P., Johnson, M. J., Leary, C., Maclaurin, D., Necula, G., Paszke, A., VanderPlas, J., Wanderman-Milne, S., and Zhang, Q., "JAX: composable transformations of Python+NumPy programs," , 2018. URL http://github.com/jax-ml/jax.

[31] Kidger, P., "On Neural Differential Equations," Ph.D. thesis, University of Oxford, 2021.

[32] Jones, E., Oliphant, T., Peterson, P., et al., "SciPy: Open source scientific tools for Python," , 2001–. URL http://www.scipy.org/.

[33] Blondel, M., Berthet, Q., Cuturi, M., Frostig, R., Hoyer, S., Llinares-López, F., Pedregosa, F., and Vert, J.-P., "Efficient and Modular Implicit Differentiation," *arXiv preprint arXiv:2105.15183*, 2021.

[34] Söderlind, G., "Digital Filters in Adaptive Time-Stepping," *ACM Transactions on Mathematical Software*, Vol. 20, No. 1, 2003, pp. 1–26.

[35] Gámez Losada, F., Visser, P., and Heiligers, M., "Estimating the Performance of Patched Multirevolution Solar-Sail Transfers Around Planets," *Journal of Guidance, Control, and Dynamics*, 2025, pp. 1–12. https://doi.org/10.2514/1.G009233, URL https://doi.org/10.2514/1.G009233.

[36] Buckingham, E., "On Physically Similar Systems; Illustrations of the Use of Dimensional Equations," *Phys. Rev.*, Vol. 4, 1914, pp. 345–376. https://doi.org/10.1103/PhysRev.4.345, URL https://link.aps.org/doi/10.1103/PhysRev.4.345.

[37] Encyclopedia of Mathematics, "Condition number," http://encyclopediaofmath.org/index.php?title=Condition_number&oldid=50975, 2020. [Online; accessed 14-November-2025].

4

Conclusions and Recommendations

The focus of this thesis is to set up an indirect optimization framework to solve planar planetocentric circular-to-circular (C2C) solar-sail transfer optimal control problems (OCPs). Additionally, fundamental characterization of these types of transfers is given, and the optimization framework is analyzed for sensitivity, convergence, and robustness. The conclusions with reference to the research questions defined in Section 2.4.2 are given in Section 4.1, and the recommendations for future work are given in Section 4.2.

4.1. Conclusions

The conclusions are given in an answer format to the research questions posed in Section 2.4.2, and a general discussion is written with reference to the research objective.

- RQ1: *How can the planar circular-to-circular (C2C) solar-sail transfer around a planetary body be posed as a TPBVP using calculus of variations (CoV) and Pontryagin's Maximum Principle (PMP)?*

  In this work, the problem is successfully posed as a two-point boundary value problem (TPBVP) using calculus of variations (CoV) and Pontryagin's Maximum Principle (PMP), following the steps from [37], [38]. To begin with, the equations of motion are written out using the polar coordinate system. After deriving the dynamics, the objective and constraints of the problem are determined. In this case, the objective is to maximize the orbital radius over a given duration while keeping the terminal orbit circular. Then, the Hamiltonian is written out, which introduces a set of costates and ties the system's dynamics into the objective. The co-state dynamics are then derived using the Euler-Lagrange equations. Then, perhaps most importantly, the PMP is used, which states that the optimal control input minimizes the Hamiltonian at each point along the trajectory. By isolating the components of the Hamiltonian that depend on control, a primer vector direction can be defined through costates in which the acceleration must be maximized. An analytical expression exists that allows determination of the required cone and clock angles based on the primer vector direction [1]. As a result of this, the control inputs are written as a function of the costates and do not appear in the problem formulation. To determine the terminal boundary conditions of the costates, a terminal function is set up that introduces two constant Lagrangian multipliers corresponding to the two terminal circularity constraints. After that, there are four states, four costates, and two Lagrangian multipliers, together with eight differential equations, eight boundary conditions, and two algebraic side conditions, which can be set up as a TPBVP and solved using a shooting method.
- RQ2: *How does the defined optimization algorithm perform, when applied to the identification of optimal planar circular-to-circular (C2C) solar-sail transfers?*

  The defined optimization framework can effectively solve many-revolution transfers with either time or anomaly as the independent variable. Further details are given in the following subques-

tions.

- RQ2a: *How does an indirect shooting-method solution compare against a state-of-the-art direct collocation solver (e.g., GPOPS-II) in terms of convergence robustness, computational cost, and solution accuracy for single-revolution transfers?*

  The indirect optimization results for a variety of transfer configurations are compared against a state-of-the-art direct collocation solver (GPOPS-II) to validate the defined optimization framework. Across all comparisons, the outputs of the indirect method closely match the GPOPS-II baseline, and the radius gain is marginally above the GPOPS-II reference value, as expected.

  No quantitative analysis is done on differences in convergence, sensitivity, and robustness between the indirect and direct solvers. The main reason for this is the difficulty of comparing the initial guess quality of the two methods, with the indirect framework requiring just the guess of the co-state and Lagrangian multiplier values at the initial state, and the direct framework requiring a guess of the full state and control profile of the whole transfer. Instead, an independent analysis is performed on the indirect method alone, focusing on the sensitivity of the solution elements with reference to problem inputs and the convergence characteristics with reference to the solver, independent variable choice, and problem inputs.

  The indirect method was analysed in terms of both sensitivity and convergence. It was shown that, in general, the solution elements (the initial values of the four costates and the two constant Lagrange multipliers) vary smoothly with the transfer parameters. This behaviour indicates that continuation methods can be used effectively to reach convergence for difficult transfer configurations that would otherwise not converge from a trivial initial guess. The convergence analysis further revealed that increasing the transfer duration improves convergence, owing to better conditioning of the residual-function Jacobian. In addition, low-inclination transfers exhibit smaller convergence basins due to poor illumination conditions, and lower initial-radius values perform worse than higher initial-radius values. Finally, it was shown that the direction of the primer vector in the initial guess is more important for convergence than its magnitude.

- RQ2b: *How do key sail performance parameters and orbital geometry affect existence, uniqueness, and performance of the optimal C2C solution?*

  In the given work, a formal analysis of existence and uniqueness is not performed. In practice, any trajectory for which the solver reported convergence with terminal residuals small enough is accepted as a converged solution. Instead, a full analysis is performed on the effect of sail performance and orbital geometry on the transfer performance of the optimal solution.

  It was demonstrated that the transfer performance (i.e., radius change over initial radius, $\mathcal{P} = \Delta r / r_0$) is highly dependent on the start-phase, ϕ_0, which defines the start time of the transfer relative to the primary's orbit around the Sun, or in other words, theorientation of the orbital plane with reference to the Sun-line at the initial time step. It was found that, for a given transfer duration, there exist two ϕ_0 values that lead to the best transfer performance and two ϕ_0 values that lead to the worst transfer performance. The performance is best when the Sun-line becomes perpendicular to the line of nodes at the transfer's midpoint, while performance is worst when the Sun-line becomes parallel to the line of nodes at the transfer's midpoint. This effect is dominant for high-inclination orbits with respect to the ecliptic ($i = 90°$) and negligible for low-inclination orbits ($i = 0°$) due to the latter having constant illumination conditions at all times. Additionally, it was found that, when the duration of the transfer is less than a year, the best-phased $i = 90°$ cases have the largest radius gain. For transfer times near a year, lower-inclination transfers outperform the $i = 90°$ case.

  Dimensional analysis was used to reduce the problem's five-dimensional input space into three independent Π-groups: Π_a, Π_r, and Π_t. Each group contains only one of the primary mission design variables (acceleration, radius, or time), enabling isolated variation of each variable. Numerical analysis revealed a simple power-law relationship for transfer perfor-

mance: $\mathcal{P} \propto \Pi_a^{1.0}\Pi_r^{0.5}$. This model was shown to accurately extrapolate performance across different sail designs (a_0) and initial altitudes (r_0) from a single benchmark optimization, providing an effective tool for first-order trade-off studies.

As a general conclusion, it can be said that the planar planetocentric C2C solar-sail transfer problem was successfully written as a TPBVP and solved using shooting methods. Additionally, the resulting optimization framework was characterized, and the optimal C2C solutions were analyzed, providing a strong base for future studies to extend the indirect optimization framework for similar transfers.

4.2. Recommendations

This study establishes an indirect optimization baseline for planar planetocentric C2C solar-sail transfers. That being said, there are multiple limitations and possible extensions that point to the next research steps.

Modelling and Physics

Current work focused on planar optimal C2C transfers using an ideal sail model. Therefore, future work could start by removing these assumptions. Extending the current framework to 3D dynamics and using a non-ideal sail model (i.e., optical sail model) would bring the solutions closer to reality and also validate the found trends in a more realistic scenario. Additionally, it is recommended that future studies include eclipses, third-body gravity, and higher-order perturbations that were neglected in the current work. In terms of the control input, realistic control and actuation limits (i.e., maximum slew rate) could be introduced, which were not enforced in the present work. Finally, future efforts could move beyond the C2C boundary conditions into more general boundary conditions, allowing elliptical transfers and plane-change problems to assess performance on realistic mission cases.

Algorithms and Solvers

This paper implemented an indirect optimization framework and solved it using single shooting. It is recommended that future work implement the PMP-DDP framework to address sensitivity and robustness as done in [48]. This thesis planned such work but did not execute it, making this the most direct next step. Additionally, multiple shooting could be implemented to widen the convergence basins. As an extension of the sensitivity and convergence work done in this paper, future studies could further analyze the Jacobian of the shooting residuals to uncover patterns between the initial guess elements and the residual vector elements, perhaps leading to a more informed way to generate initial guesses for the OCP. Finally, it is recommended to extend the current problem formulation to include flexible final time, allowing the user to specify a target radius and minimize the transfer time.

Indirect-Direct Optimization Comparison

Future studies are encouraged to extend the numerical verification between indirect and direct frameworks for the given problem. No comprehensive quantitative way to compare the two methods was found in this paper, but a comparative study analyzing runtime, convergence, and sensitivity would solidify the indirect method and its use cases.

Design-oriented analysis

With the proportional scaling law in acceleration and radius, it is recommended to further study the effect of phasing to characterize that using simple analytical expressions, as was done for the scaling law in this study. This would allow for extrapolation of transfer performance through every parameter in the problem setup.

References

[1] C. R. McInnes, “Solar sailing: Technology, dynamics and mission applications,” 1999.

[2] M. Macdonald, “Solar sailing: Applications and technology advancement,” 2011. DOI: 10.5772/13614.

[3] H. Sawada, O. Mori, N. Okuizumi, *et al.*, “Mission report on the solar power sail deployment demonstration of ikaros,” 2011. DOI: 10.2514/6.2011-1887.

[4] W. K. Wilkie, “Overview of the nasa advanced composite solar sail system (acs3) technology demonstration project,” in *AIAA Scitech 2021 Forum*. DOI: 10.2514/6.2021-1260. eprint: https://arc.aiaa.org/doi/pdf/10.2514/6.2021-1260. [Online]. Available: https://arc.aiaa.org/doi/abs/10.2514/6.2021-1260.

[5] M. Otten and C. McInnes, “Near minimum-time trajectories for solar sails,” 2001. DOI: 10.2514/2.4758.

[6] B. Dachwald, G. Mengali, A. Quarta, and M. Macdonald, “Parametric model and optimal control of solar sails with optical degradation,” 2006. DOI: 10.2514/1.20313.

[7] G. Mengali and A. A. Quarta, “Solar sail trajectories with piecewise-constant steering laws,” *Aerospace Science and Technology*, 2009. DOI: 10.1016/j.ast.2009.06.007.

[8] A. A. Quarta, G. Mengali, and M. Bassetto, “Optimal solar sail transfers to circular earth-synchronous displaced orbits,” *Astrodynamics*, 2020. DOI: 10.1007/s42064-019-0057-x.

[9] M. Macdonald and C. McInnes, “Realistic earth escape strategies for solar sailing,” 2005. DOI: 10.2514/1.5165.

[10] M. Macdonald and C. McInnes, “Analytical control laws for planet-centered solar sailing,” 2005. DOI: 10.2514/1.11400.

[11] D. A. Spencer, B. Betts, J. Bellardo, A. Diaz, B. Plante, and J. R. Mansell, “The lightsail 2 solar sailing technology demonstration,” *Advances in Space Research*, 2021. DOI: 10.1016/j.asr.2020.06.029.

[12] T. Tsu, “Interplanetary travel by solar sail,” 1959. DOI: 10.2514/8.4791.

[13] N. Sands, “Escape from planetary gravitational fields by use of solar sails,” 1961. DOI: 10.2514/8.5547.

[14] K. Oguri, G. Lantoine, A. E. Petropoulos, and J. W. McMahon, “Solar sailing q-law for planetocentric, many-revolution sail orbit transfers,” *Journal of Guidance Control and Dynamics*, 2023. DOI: 10.2514/1.g007103.

[15] D. Morante, M. S. Rivo, and M. Soler, “A survey on low-thrust trajectory optimization approaches,” *Aerospace*, 2021. DOI: 10.3390/aerospace8030088.

[16] P. Kelly and R. Bevilacqua, “Geostationary debris mitigation using minimum time solar sail trajectories with eclipse constraints,” *Optimal control applications & methods*, 2020. DOI: 10.1002/oca.2676.

[17] A. D. Iuliis, F. Ciampa, L. Felicetti, and M. Ceriotti, “Sailing with solar and planetary radiation pressure,” *Advances in Space Research*, 2021. DOI: 10.1016/j.asr.2019.11.036.

[18] G. Mengali and A. Quarta, “Near-optimal solar-sail orbit-raising from low earth orbit,” 2005. DOI: 10.2514/1.14184.

[19] L. Carzana, P. Visser, and J. Heiligers, “Delft university of technology solar-sail control laws for perturbed earth-bound trajectories,” 2021.

[20] L. Carzana, P. N. A. M. Visser, and M. J. Heiligers, “Locally optimal control laws for earth-bound solar sailing with atmospheric drag,” *Aerospace Science and Technology*, 2022. DOI: 10.1016/j.ast.2022.107666.

[21] G. Ambrosio, "Characterizing minimum-time collision avoidance maneuvers for solar sails in earth orbit," M.S. thesis, TU Delft, 2025.

[22] V. Gottumukkala, "Assessing the collision-avoidance capability of solar sails in low earth orbit," M.S. thesis, TU Delft, 2025.

[23] K. Oguri and G. Lantoine, "Indirect trajectory optimization via solar sailing primer vector theory: Minimum solar-angle transfers," *Acta Astronautica*, 2023. DOI: 10.1016/j.actaastro.2023.06.032.

[24] L. L. Sackett, "Optimal solar sail planetocentric trajectories," *NASA STI/Recon Technical Report N*, 1977.

[25] L. L. Sackett, "Sunspot: A computer program for producing optimal solar sail planetocentric trajectories," *NASA STI/Recon Technical Report N*, 1977.

[26] V. Coverstone and J. Prussing, "Technique for escape from geosynchronous transfer orbit using a solar sail," 2003. DOI: 10.2514/2.5091.

[27] V. Stolbunov, M. Ceriotti, C. Colombo, and C. McInnes, "Optimal law for inclination change in an atmosphere through solar sailing," 2013. DOI: 10.2514/1.59931.

[28] C. Bianchi, L. Niccolai, G. Mengali, and M. Ceriotti, "Preliminary design of a space debris removal mission in leo using a solar sail," *Advances in Space Research*, 2024. DOI: 10.1016/j.asr.2024.01.024.

[29] P. Kelly and R. Bevilacqua, "An optimized analytical solution for geostationary debris removal using solar sails," *Acta Astronautica*, 2019. DOI: 10.1016/j.actaastro.2019.05.055.

[30] A. Barles, M. Ceriotti, F. Ciampa, and L. Felicetti, "An optimal steering law for sailing with solar and planetary radiation pressure," *Aerospace Science and Technology*, 2021. DOI: 10.1016/j.ast.2021.107051.

[31] G. Leemans, L. Carzana, and M. J. Heiligers, "Many-revolution earth-centred solar-sail trajectory optimisation using differential dynamic programming," *AIAA SCITECH 2022 Forum*, 2022. DOI: 10.2514/6.2022-1776.

[32] R. Fitzgerald, "Characterizing minimum-time solar sail geostationary orbit transfers using pseudospectral optimal control," *Journal of Spacecraft and Rockets*, 2021. DOI: 10.2514/1.a34950.

[33] F. G. Losada, P. N. A. M. Visser, and M. J. Heiligers, "Fundamentals of solar-sail transfers around planetary bodies," *Fundamentals of Solar-Sail Transfers Around Planetary Bodies*, 2024.

[34] R. Minnozzi, "Differential dynamic programming for the optimization of many-revolution solar-sail transfers," M.S. thesis, TU Delft, 2025.

[35] B. A. Conway, "A survey of methods available for the numerical optimization of continuous dynamic systems," *Journal of Optimization Theory and Applications*, 2012. DOI: 10.1007/s10957-011-9918-z.

[36] F. Topputo and C. Zhang, "Survey of direct transcription for low-thrust space trajectory optimization with applications," *Abstract and Applied Analysis*, vol. 2014, no. 1, p. 851 720, 2014. DOI: https://doi.org/10.1155/2014/851720. eprint: https://onlinelibrary.wiley.com/doi/pdf/10.1155/2014/851720. [Online]. Available: https://onlinelibrary.wiley.com/doi/abs/10.1155/2014/851720.

[37] J. M. Longuski, J. J. Guzmán, and J. E. Prussing, "Optimal control with aerospace applications," *Springer eBooks*, 2014. DOI: 10.1007/978-1-4614-8945-0.

[38] H. Weinert, "Bryson, a. e./ ho, y.-c., applied optimal control, optimization, estimation, and control. new york-london-sydney-toronto. john wiley & sons. 1975. 481 s., £10.90," *ZAMM - Journal of Applied Mathematics and Mechanics / Zeitschrift für Angewandte Mathematik und Mechanik*, vol. 59, no. 8, pp. 402–402, 1979. DOI: https://doi.org/10.1002/zamm.19790590826. eprint: https://onlinelibrary.wiley.com/doi/pdf/10.1002/zamm.19790590826. [Online]. Available: https://onlinelibrary.wiley.com/doi/abs/10.1002/zamm.19790590826.

[39] J. Betts, "Survey of numerical methods for trajectory optimization," 1998. DOI: 10.2514/2.4231.

[40] L. Dixon and M. C. Biggs, “The advantages of adjoint-control transformations when determining optimal trajectories by pontryagin’s maximum principle,” *The Aeronautical Journal (1968)*, 1972. DOI: 10.1017/s0001924000042731.

[41] H. Yan and H. Wu, “Initial adjoint variable guess technique and its application in optimal orbital transfer,” *Journal of Guidance Control and Dynamics*, 1999. DOI: 10.2514/2.7631.

[42] E. Taheri, N. Li, and I. Kolmanovsky, “Co-state initialization for the minimum-time low-thrust trajectory optimization,” *Advances in Space Research*, 2017. DOI: 10.1016/j.asr.2017.02.010.

[43] D. Wu, W. Wang, and F. Jiang, “Minimum-time low-thrust many-revolution geocentric trajectories with analytical costates initialization,” *Aerospace Science and Technology*, 2021. DOI: 10.1016/j.ast.2021.107146.

[44] A. A. Quarta, “Initial costate approximation for rapid orbit raising with very low propulsive acceleration,” *Applied Sciences*, 2024. DOI: 10.3390/app14031124.

[45] A. A. Quarta, “Fast initialization of the indirect optimization problem in the solar sail circle-to-circle orbit transfer,” *Aerospace Science and Technology*, 2024. DOI: 10.1016/j.ast.2024.109058.

[46] K. Wang, F. Lu, Z. Chen, and J. Li, “A physics-informed indirect method for trajectory optimization,” *arXiv (Cornell University)*, 2024. DOI: 10.48550/arxiv.2402.00339.

[47] Y. Sidhoum and K. Oguri, “Indirect forward-backward shooting for low-thrust trajectory optimization in complex dynamics,” *Journal of guidance, control, and dynamics*, 2024. DOI: 10.2514/1.g007997.

[48] Y. Sidhoum and K. Oguri, “Pontryagin-bellman differential dynamic programming for low-thrust trajectory optimization with path constraints,” 2025.

[49] M. A. Patterson and A. V. Rao, “Gpops-ii: A matlab software for solving multiple-phase optimal control problems using hp-adaptive gaussian quadrature collocation methods and sparse nonlinear programming,” *ACM Trans. Math. Softw.*, vol. 41, no. 1, Oct. 2014, ISSN: 0098-3500. DOI: 10.1145/2558904. [Online]. Available: https://doi.org/10.1145/2558904.

5

Project Management

This section outlines the work breakdown structure (WBS) for the thesis project. The work was initially divided into 6 work packages to ensure a systematic and timely completion of the research objectives. A correction was made at the mid-term meeting regarding the contents of WP4. The updated contents are given separately, time allocations were not changed.

WP1: Mathematical Formulation (13 days)

- **Equations of Motion Formulation (3 days):** Formulate the planetocentric solar sailing equations of motion in cartesian and polar coordinates and additionally using mean equinoctal elements.
- **TPBVP Formulation (5 days):** Formulate the circular-to-circular solar-sail transfer problem using calculus of variations and Pontryagin's Maximum Principle.
- **Documentation (2 days):** Report results in the thesis document.
- **Margin (3 days):** A margin is left in case solution methods have difficulty converging and an alternative formulation of the problem (change of variables, different coordinate frame) is necessary.

WP2: Implementation of Numerical Methods (10 days)

- **Propagator Implementation (4 days):** Set up the propagator to propagate the dynamics inside of the solver algorithm.
- **Solver Implementation (4 days):** Implement indirect shooting methods to solve the TPBVP.
- **Margin (2 days):** A relatively small margin is left because both algorithms already have existing frameworks available in literature.

WP3: Experimentation, Analysis, and Validation (40 days)

- **Perform Optimization (5 days):** Run optimizations for single-revolution transfers using implemented methods.
- **Analysis and Discussion (15 days):** Analyze data and describe the found control laws/control regimes.
- **Comparative Analysis (10 days):** Evaluate convergence, computational cost, and solution accuracy between indirect and direct methods.
- **Documentation (5 days):** Report results in the thesis document.
- **Margin (5 days):** This step has the highest uncertainty due to the high possibility that the optimization does not converge and adjustments to the problem formulation are needed.

WP4: Analysis of Novel Solution Methods (16 days)

- **Implement DDP TPBVP Solver (5 days):** Implement the DDP TPBVP solver demonstrated in [48].

- **Comparative Analysis (5 days):** Evaluate convergence, computational cost, and solution accuracy between DDP, indirect and direct methods.
- **Documentation (3 days):** Report results in the thesis document.
- **Margin (3 days):** Possible errors and setbacks may arise due to the DDP solver being a novel solution method.

Updated WP4: Analysis of the Indirect Framework (16 days)

- **Sensitivity Analysis (5 days):** Evaluate the sensitivity of the solution elements with reference to the problem inputs.
- **Convergence Analysis (7 days):** Evaluate convergence of different problem geometries to quantify the robustness of the developed framework.
- **Documentation (3 days):** Report results in the thesis document.
- **Margin (1 days):** Small margin for delays in computation.

WP5: Expansion to Many Revolution Transfers (28 days)

- **Simulation and Experimentation (10 days):** Start with simplified situations and build to more complex dynamics, get the optimizer to converge on many-revolution transfers.
- **Analysis and Discussion (10 days):** Analyze the results and describe the control laws. Compare the resulting control laws to the control laws from the single revolution transfer.
- **Documentation (5 days):** Report results in the thesis document.
- **Margin (3 days):** Difficulties may arise in getting the optimizer to converge.

WP6: Documentation (18 days)

- **Report WP1 (1 day):** Report WP1.
- **Report WP2 (1 day):** Report WP2.
- **Report WP3 (2 days):** Report WP3.
- **Report WP4 (2 days):** Report WP4.
- **Report WP5 (2 days):** Report WP5.
- **Final Adjustments (1 day):** Final adjustments before submission.
- **Implementing Feedback (6 days):** Feedback Implementation.
- **Margin (3 days):** Margin left for feedback and writing.

A tabular overview of the work packages together with time allocations is given in Table 5.1.

Table 5.1: Time Allocation by Work Package

Work Package	Nominal Time (days)	Margin (days)
Literature Study	35	0
WP1: Mathematical Formulation	10	3
WP2: Implementation of Numerical Methods	8	2
WP3: Experimentation, Analysis, and Validation	35	5
Midterm Review		
WP4: Analysis of Novel Solution Methods	13	3
WP4*: Analysis of the Indirect Framework	15	1
WP5: Expansion to Many-Revolution Transfers	25	3
WP6: Documentation	15	3
Total	**141 (28.2 weeks)**	**19 (3.8 weeks)**

6

Verification and Validation

Verification

The implementation of the method was verified by checking the frame rotation correctness, boundary conditions, dynamics behavior in controlled limits, and self-consistency of derived quantities (eccentricity, control). Tests are automated with `pytest` and use the same numerical stack as the solver (JAX, Diffrax). The overview of implemented tests is given in Table 6.1. All tests passed under the stated tolerances.

Table 6.1: Unit-test overview for the solar-sailing indirect trajectory solver.

ID	What it checks	Method	Pass criterion
T1	Rotation matrices are orthonormal and proper	Build $R_{\mathsf{rtn}\to\mathsf{slf}}$ at several samples; verify $R^\top R \approx I$ and $\det(R) \approx 1$.	$\|R^\top R - I\|_{\mathsf{F}} < 1\mathrm{e}{-10}$; $\|\det(R) - 1\| < 1\mathrm{e}{-10}$
T2	Terminal constraint for circular target is zero	Evaluate terminal constraint on state $(r_{\mathsf{bar}}, u_{\mathsf{bar}}, v_{\mathsf{bar}}) = (1, 0, 1)$.	Both components $< 1\mathrm{e}{-12}$
T3	Zero-thrust circular equilibrium (true-anomaly form)	Set characteristic acceleration $a_0 = 0$; integrate over one revolution; track $(r_{\mathsf{bar}}, u_{\mathsf{bar}}, v_{\mathsf{bar}})$.	$\max\|r_{\mathsf{bar}} - 1\| < 1\mathrm{e}{-8}$; $\max\|u_{\mathsf{bar}}\| < 1\mathrm{e}{-8}$; $\max\|v_{\mathsf{bar}} - 1\| < 1\mathrm{e}{-8}$
T4	Zero-thrust circular equilibrium (time form)	Set $a_0 = 0$; integrate over one period; track $(r_{\mathsf{bar}}, u_{\mathsf{bar}}, v_{\mathsf{bar}})$.	Same criteria as T3
T5	Control direction equals acceleration direction in Sun-line frame	Compute unit vector control in SLF; independently rotate thrust acceleration to the Sun-line frame and normalize; compare directions.	Angle (or vector) mismatch $< 1\mathrm{e}{-8}$
T6	Control never points towards the Sun	Compute unit vector control in SLF; check u_x.	$u_x > 0$.
T7	Shooting Jacobian well-formed	Form the shooting Jacobian at a nominal point; check shape and finiteness.	Shape 6×6; all entries finite

Validation

The indirect method solution was validated by comparing it against a direct collocation solution (GPOPS-II [49]) for the same boundary-value problem and parameters. For better visualization, the last two revolutions of a 10-revolution, GEO altitude, $0.1\ \mathrm{mm/s^2}$ characteristic acceleration, 90° RAAN, 45° inclination transfer are visualized. The planar positions are shown in Figure 6.1a, velocities in Figure 6.1b, and the cartesian accelerations in Figure 6.1c. Across all comparisons, the outputs of the indirect method closely match the GPOPS-II baseline and the radius gain is marginally above the GPOPS-II reference value as expected. These results validate both the dynamics and frame transformations of the indirect implementation.

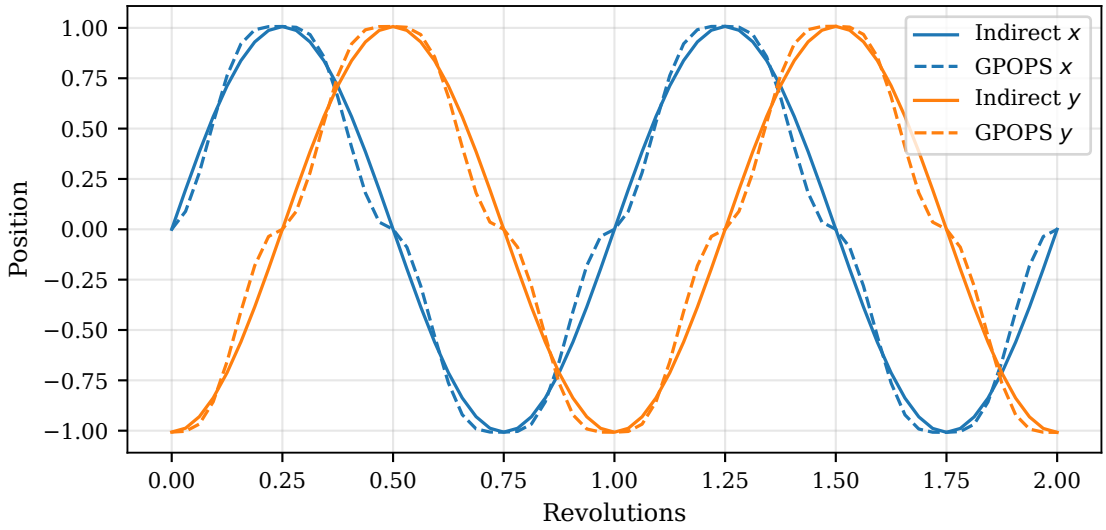

(a)

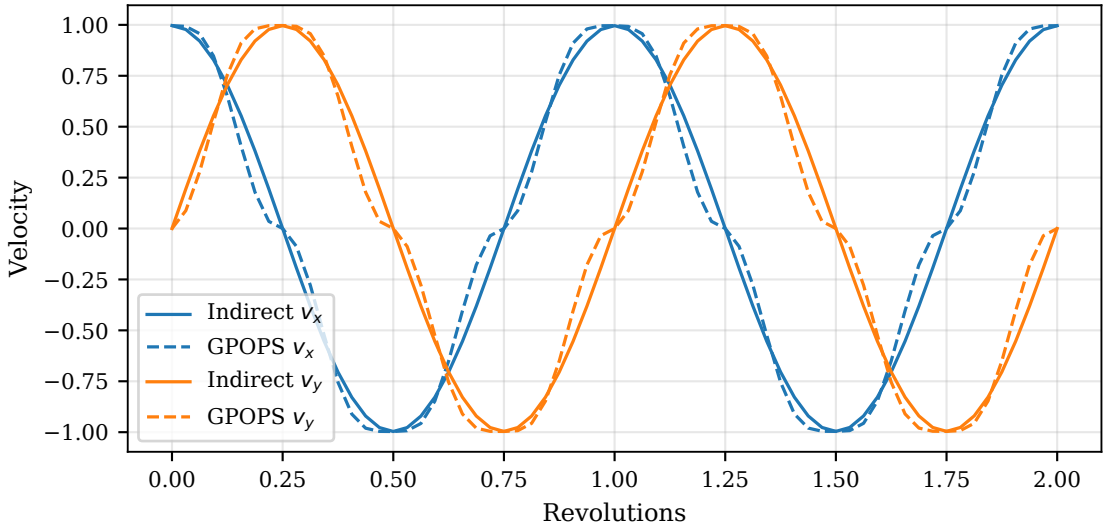

(b)

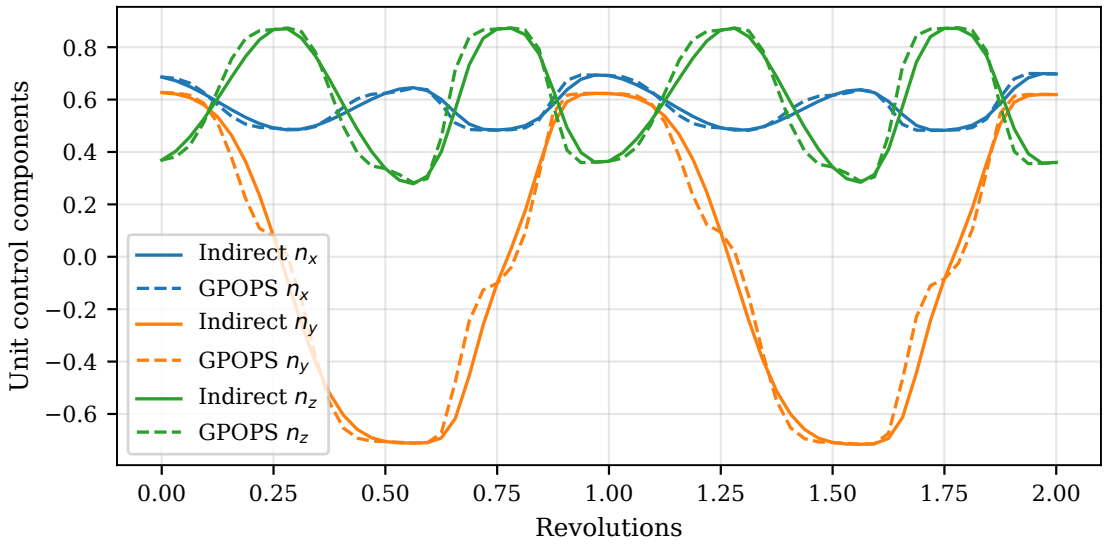

(c)

Figure 6.1: The last two revolutions of a 10-revolution transfer for both GPOPS-II and indirect optimization: a) planar position, b) planar velocity, and c) cartesian acceleration.